Pergamon

0301-9322(93)E0030-9

*Int. J. Multiphase Flow* Vol. 20, No. 3, pp. 453–479, 1994

0301-9322/94 $7.00 + 0.00

# PHASE DISTRIBUTION AND TURBULENCE STRUCTURE FOR SOLID/FLUID UPFLOW IN A PIPE

A. ALAJBEGOVIĆ, A. ASSAD, F. BONETTO and R. T. LAHEY JR
Center for Multiphase Research, Rensselaer Polytechnic Institute, Troy, NY 12180, U.S.A.

*(Received 13 October 1992; in revised form 13 December 1993)*

**Abstract**—The phase distribution and turbulence structure for solid/fluid upflow in a vertical pipe were investigated. Spherical particles, approximately 2 mm in diameter, were used and runs were made with particles having two different specific gravities. In particular, ceramic particles, which were heavier than water, and expanded polystyrene particles, which were lighter than water, were used. A new method is presented for the measurement of the volume fraction in solid/fluid two-phase flows using a laser-Doppler anemometer (LDA). The measured local time fractions obtained with the LDA must be corrected, because bias is produced by the presence of natural seeding, the finite size of the measurement volume and interruptions of the laser beams by the dispersed particles. An analytical method has been developed which accounts for these effects. A single-beam traversing $\gamma$-ray densitometer was used as a reference against which to assess the volume fraction correction method. Good agreement between the corrected LDA and $\gamma$-ray densitometer results was obtained. The volume fraction profiles show that at low flow rates the ceramic particles have an almost uniform distribution, while increasing the flow rate causes coring. In contrast, the phase distribution of the light polystyrene particles had wall peaking for both the low and high flow rates. However, wall peaking was flattened as liquid flow rate was increased.

*Key Words:* two-phase turbulence, solid/fluid flow, slurries, LDA

## 1. INTRODUCTION

The transport of solid/fluid mixtures is an important phenomenon in many industrial applications. Much has been published, including both theoretical analyses and experimental data. However, relatively few experiments have been done for solid/fluid flows having relatively large particles. Detailed measurements in flowing solid/fluid systems are very difficult to perform, since most intrusive instrumentation is not applicable. The main parameters of interest are the local volume fraction, the mean velocities, the turbulence intensity and the Reynolds stress distribution for both phases. Detailed measurements are important for the understanding of the physical mechanisms which control the phase distribution processes in solid/fluid flows. Moreover, in solid/fluid flows light dispersed particles can be used to simulate bubbles. In this way, the effect of bubble shape and specific gravity on the lateral distribution of the dispersed phase can be studied. This is particularly important for the assessment of multidimensional two-fluid models.

Phase distribution phenomena in two-phase flow is a challenging problem, since the phase interactions are not completely understood. Serizawa (1974) measured the lateral void distribution and the turbulent structure of the liquid phase for air/water upflow in a vertical pipe. His void distribution data showed wall peaking for bubbly flows, evolving into void coring (i.e. internal peaking) as the global void fraction increased and slug flow occurred. Wang *et al.* (1987) also made detailed measurements for upward and downward bubbly flows and found wall peaking of the void fraction for bubbly upflows and void coring for bubbly downflows. These data imply that the buoyancy of the dispersed phase plays an important role in determining the lateral phase distribution. Experimental results by Žun (1985), and others, have shown that bubble size and shape also affect the phase distribution. Indeed, small bubbles tend to concentrate near the wall, while larger bubbles migrate towards the pipe's centreline, resulting in coring.

Akagawa *et al.* (1989) have performed measurements in particle/water flows using spherical particles, which were approximately 2 mm in diameter. They used an intrusive, reflective type, optical fiber sensor for both velocity and volume fraction measurements in vertical pipe upflows. The particles had three different densities: lighter, heavier and the same as the density of water.

Their experiments were done at relatively low liquid superficial velocities, $\langle j_L \rangle \leqslant 1.0$ m/s, and for global particle volume fractions up to 6%. They observed both wall peaking and coring in the measured volume fraction distribution.

Sakaguchi *et al.* (1991) used a high-speed camera for the measurement of volume fraction and particle velocity. These measurements were done using aluminum ceramic spheres which were 4 mm in diameter, had a liquid velocity ranging between $\langle j_L \rangle = 1.0$ to 2.5 m/s and a global volume fraction in the range $\langle \epsilon \rangle = 0.5$ to 1.5%. They observed particle coring at high velocities but, unexpectedly, wall peaking occurred at low velocities. Unfortunately, neither of the Japanese experiments include measurements of the turbulence structure and the Reynolds stress distribution, thus complete assessment of multidimensional two-fluids models is not possible.

In the present study, the lateral phase distribution and detailed measurement of the velocity field were done for vertical upflows in a pipe. The particles used were approximately 2 mm in diameter and had two different densities (see table 1). A DANTEC fiber flow laser-Doppler anemometer (LDA) system gave accurate measurements of the local velocity, turbulence intensity and Reynolds stresses for both the solid and liquid phases. The combination of the LDA data, the correction method described in this paper and a single-beam $\gamma$-ray densitometer, also allowed for the accurate determination of the volume fraction distribution of the dispersed solid phase.

The measurement of solid/fluid two-phase flows represents a difficult challenge, since nonintrusive methods have to be applied. Fortunately, an LDA seems to be an ideal device for such measurements. Durst & Zaré (1975) were apparently the first to report that satisfactory LDA signals could be obtained with large spherical particles. Since then, a lot of work has been done to measure particle velocity, size and number density. Wigley (1978) measured the size and velocity of large water droplets by using a dual-beam LDA system, in which the transit time could be measured by observing the reflections from the droplets. Farmer (1972, 1974, 1980) and Saffman (1987) developed models to measure the particle number density. Moreover, Saffman (1987) presented a method for the measurement of the local volume fraction using an LDA system. Unfortunately, this method is only valid for small spherical particles.

It is of great interest to know the spatial distribution of the volume fraction of the solid phase (i.e. the particles) in a conduit. This important parameter can be measured by taking the sum of all the particle transit times, $t_j$, at the particular location, $\mathbf{r}$, and dividing by the total measurement time, $T$:

$$\epsilon(\mathbf{r}) = \frac{\sum_{j=1}^{N} t_j(\mathbf{r})}{T}. \qquad [1]$$

It should be noted that by integrating [1] over the pipe's cross-sectional area the average volume fraction, $\langle \epsilon \rangle$, can also be obtained.

An LDA system can be used to measure the local volume fraction of large particles based on [1]. However, these results are biased because of the following reasons:

(1) The LDA simultaneously measures both the large and small particles (i.e. seeding) which are present in the fluid phase. The transit time of the seeding contributes to the particle volume fraction, making it larger.
(2) The LDA measurement volume is finite in size, instead of just measuring at one point. Hence, the inferred volume fraction represents an integration over the measurement volume.
(3) The laser beam is interrupted by the solid particles between the laser source and the measurement volume. Whenever the beam is interrupted, the system is unable to measure and the effective measuring time is reduced. Since the actual time of measurement is larger than the effective one, [1] leads to a smaller measured volume fraction than the actual one.

In order to measure the local volume fraction of the large particles with an LDA, the experimentally obtained results must be corrected for the above effects. The data correction method presented herein is valid for dilute slurries of solid spherical particles and liquid.

## 2. EXPERIMENTAL METHOD

The velocity and volume fraction distribution were measured with a state-of-the-art LDA system. All the components of the LDA system, except the laser, were made by DANTEC Electronics. A Spectra-Physics (Stabilite 2016) argon ion laser was used as the source of coherent light. The principles of operation of an LDA have been described extensively in the literature (Durst *et al.* 1981; Durrani & Greated 1977) and are not repeated here. The LDA probe was placed in the water tank with the test section. It consisted of a submersible two-dimensional fiber optic probe, a beam expander and a sealed glass window, which was used to prevent lens abberration. The probe was mounted on a three-dimensional traversing mechanism, which allowed full probe positioning in all three orthogonal directions with a position accuracy of $\pm 1\ \mu$m. The LDA system was operated in the backscatter mode. The whole process was controlled by an IBM AT microcomputer via an IEEE 488 interface. The same microcomputer was used for data acquisition and processing. Table 1 shows the principal characteristics of the LDA system. The test loop configurations used are shown in figures 1 and 2.

The sensitivity to noise is reduced by the use of a three-level burst detection scheme (DANTEC 1989). Level 2 determines the start and stop of the particle's transit time measurement. The integration period starts at a positive crossing of level 2 and stops at a negative crossing of level 2. The envelope must exceed level 3 for a burst to be accepted. Also, the signal must drop below level 1 before a new measurement can start. This procedure reduces the sensitivity to noise, since multiple crossings of level 2 are ignored as long as level 1 or 3 is not crossed.

The test section was made of optically clear transparent fluorinated ethylene propylene (FEP), a material with the same refraction index as water. The FEP pipe's inside diameter was $D = 30.6 \pm 0.2$ mm. The volume fraction profile was measured along the transverse $x$-axis at fixed $y$ (the $z$-axis was oriented into the flow direction). The length of the measurement volume in the $y$-direction was approximately 1 mm (see Table 1). Thus, measuring along the $y$-axis would have given biased results since they would have involved significant spatial integration. Measuring along the $x$-axis reduced this error considerably.

The particles used in these experiments were solid spheres with the characteristics shown in table 2. The ceramic particles were heavier, and the expanded polystyrene particles were lighter, than water, which was used as the continuous phase. The measured size distribution of the ceramic particles, which were used in the development of the correction method, is shown in figure 3.

There are always some impurities or natural seeding, of different sizes and shapes, present in tap water. Leaving these impurities in the loop would deteriorate the LDA signal, decrease the signal-to-noise ratio and bias the liquid velocity measurements. In this study, the amount of these impurities was reduced by the filtration of the inlet water to a level where their effect became negligible.

In the measurements of the fluid velocity special seeding was used. In particular, the liquid phase was seeded with Duke Scientific polystyrene spheres, 5 $\mu$m in diameter, with density close to that

Table 1. Principal characteristics of the LDA system

| | |
|---|---|
| Ar laser power (maximum) | 4.0 W |
| Green color wavelength[a] | 385.7 nm |
| Blue color wavelength[a] | 365.8 nm |
| Focal length of lenses | 413.5 mm |
| Beam spacing | 70.0 mm |
| Beam expansion | 1.85 |
| Laser beam diameter at $e^{-2}$ intensity | 1.35 mm |
| Half-angle of intersection | 4.84° |
| Fringe spacing | 2.287 $\mu$m |
| Frequency shift (Bragg cell) | 40 MHz |
| *Calculated dimensions of measurement volume*: | |
| Minor axis at $e^{-2}$ intensity | 0.082 mm |
| Major axis at $e^{-2}$ intensity | 0.964 mm |

[a]The green color wavelength of the Ar laser beam is 514.5 nm. Under water, this value must be divided by the index of refraction for water, 1.334. The same is true for the blue beam, whose wavelength in air equals 488 nm.

Table 2. Characteristics of the spherical particles

| Material | Sp. gr. | Mean diameter [mm] | Standard deviation [mm] |
|---|---|---|---|
| Ceramics | 2.450 | 2.32 | ±0.07 |
| Expanded polystyrene | 0.032 | 1.79 | ±0.18 |

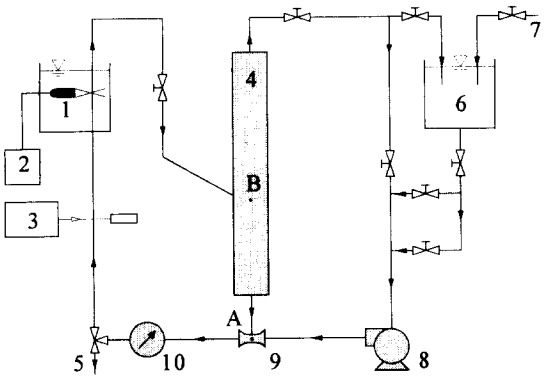


Figure 1. Schematic of the solid/liquid loop for the ceramic particles: **1,** laser probe; **2,** data acquisition; **3,** $\gamma$-densitometer; **4,** separation tank; **5,** drain; **6,** water tank; **7,** feed water; **8,** pump; **9,** Venturi; **10,** magnetic flowmeter.

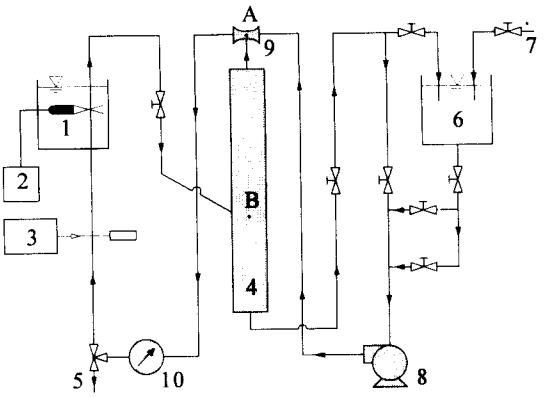


Figure 2. Schematic of the solid/liquid loop for the polystyrene particles: **1,** laser probe; **2,** data acquisition; **3,** $\gamma$-densitometer; **4,** separation tank; **5,** drain; **6,** water tank; **7,** feed water; **8,** pump; **9,** Venturi; **10,** magnetic flowmeter.

of water (i.e. sp. gr. = 1.05), resulting in optimal tagging of the liquid phase. In addition, the good scattering characteristics of the seeding increased the signal-to-noise ratio, giving reliable measurements of the liquid phase velocity.

The ratio between the particle and seeding size was approximately 1000, resulting in a large difference between the particle and seeding transit times. Hence, the measured transit time distribution clearly showed two distinct peaks. Therefore, separation between the seeding and the large particles, which comprised the dispersed phase, was easily accomplished. It will be shown that the associated error is negligible.

Two loop configurations were used, one for the heavy particles (figure 1) and the other for the light particles (figure 2). The main difference between them was in the connection of the separation tank with the rest of the loop. The particles were circulating continuously in a secondary loop, comprised of the separation tank, a Venturi and the test section, and thus they did not pass through the pump. Otherwise, they would have been destroyed (ceramic particles) or deformed (expanded polystyrene particles). The distance between the inlet into the vertical pipe at point 5, figures 1 and 2, and the test section was 2.2 m, allowing for fully developed flows.

The particles entered a separation tank after leaving the test section. The relatively large cross-sectional area of the separation tank (inner diameter of approximately 0.15 m) reduced the mixture velocity so that buoyancy became the main driving force for particle motion. The heavy ceramic particles fell downwards, continuing to the test section through the Venturi pipe at the bottom of the separation tank (figure 1). In contrast, the light expanded polystyrene particles rose upwards to the Venturi, which was placed at the top of the separation tank (figure 2). In both cases, the liquid phase returned to the pump.

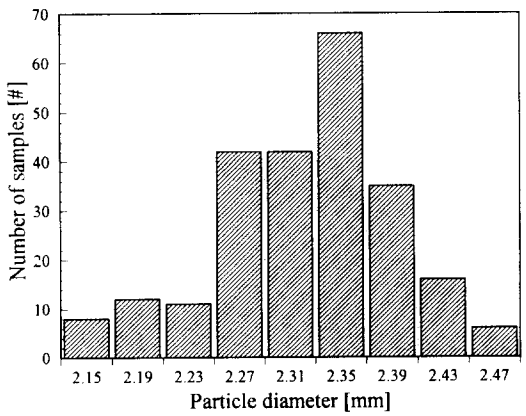


Figure 3. Size distribution of the large particles.

A calibrated magnetic flowmeter was used for the measurement of the liquid flow rate, $w$. The uncertainty of the measurement was approximately $\pm 5\%$. The same result was achieved by integrating the velocity profiles. The superficial velocities of the liquid phase, $\langle j_L \rangle$, and the solid phase, $\langle j_S \rangle$, were obtained from the integration of the measured velocity and volume fraction profiles. Since the error in the velocity measurements was negligible, the main source of uncertainty in the calculated superficial velocities was due to the error in the volume fraction results. The values for the liquid flow rate, $w$, and the superficial velocities, $\langle j_L \rangle$ and $\langle j_S \rangle$, with their uncertainties are given in tables 3 and 4.

The design of the Venturi was crucial for the proper operation of the secondary loop. The flow entering the Venturi divided into two branches, one going to the separation tank and the other to the inlet of the test section. By applying the Bernoulli equation, it can be shown that the liquid flow at the separation point is always oriented out of the Venturi (i.e. into the test section and the separation tank). To determine these velocities, the Bernoulli equation can be written for the liquid between points A and B through the test section:

$$p_A + \frac{\rho v_A^2}{2} + \rho g z_A = p_B + \frac{\rho v_B^2}{2} + \rho g z_B + \Delta p_{f,Test}. \quad [2]$$

Similarly, the Bernoulli equation for the liquid between A and B through the separation tank is

$$p_A + \frac{\rho v_A^2}{2} + \rho g z_A = p_B + \frac{\rho v_B^2}{2} + \rho g z_B + \Delta p_{f,Tank}, \quad [3]$$

where $p$ is the pressure, $\rho$ is the mixture density, $v$ is the mixture velocity, $g$ is gravity, $z$ is the height and $\Delta p_{f,Test}$ and $\Delta p_{f,Test}$ are the irreversible pressure drops through the branch containing the test section and the separation tank, respectively. These irreversible pressure drops are defined as

$$\Delta p_f = K \frac{\rho v^2}{2}, \quad [4]$$

where $K$ is the loss coefficient which accounts for both the distributed and local pressure losses in the branch, referenced to the pipe diameter at point A. Combining [2] and [3] yields

$$\Delta p_{f,Tank} = \Delta p_{f,Test}. \quad [5]$$

Using [4], [5] becomes

$$v_{Tank} = v_{Test} \sqrt{\frac{K_{Test}}{K_{Tank}}}. \quad [6]$$

The loss coefficients and the liquid velocity in the test section, $v_{Test}$, are both positive. Hence, [6] implies that liquid flows from the Venturi into the separation tank. The particles flow into the Venturi only if the liquid velocity into the tank does not exceed the particle's terminal velocity. This may occur by reducing $v_{Tank}$ through either an increase in $K_{Test}$ or a decrease in $K_{Tank}$. The Venturi was designed so that the pipe incoming from the separation tank was inserted into the high-velocity region of the Venturi. This resulted in a relatively large pressure drop for the liquid entering the separation tank, hence $v_{Tank}$ was small and the particles freely entered the secondary loop through the Venturi.

The velocities were measured in both the $r$-(radial) and $z$-(axial) directions. This required two laser beam pairs, one pair for each orthogonal direction. If all four laser beams were to be used in the measurement of the volume fraction, the effect of the beam interruptions would increase. Even if properly corrected, the resulting accuracy would be unnecessarily low. Fortunately, the

Table 3. Total mass flow rate and superficial velocities—ceramic particles

| $w$ [kg/s] | $\langle j_L \rangle$ [m/s] | $\langle j_S \rangle$ [m/s] |
|---|---|---|
| $1.095 \pm 0.055$ | $1.410 \pm 0.017$ | $0.032 \pm 0.003$ |
| $1.469 \pm 0.072$ | $1.888 \pm 0.021$ | $0.045 \pm 0.004$ |
| $1.723 \pm 0.084$ | $2.196 \pm 0.023$ | $0.060 \pm 0.005$ |

Table 4. Total mass flow rate and superficial velocities—expanded polystyrene particles

| $w$ [kg/s] | $\langle j_L \rangle$ [m/s] | $\langle j_S \rangle$ [m/s] |
|---|---|---|
| $1.060 \pm 0.052$ | $1.441 \pm 0.021$ | $0.022 \pm 0.003$ |
| $1.304 \pm 0.063$ | $1.722 \pm 0.028$ | $0.023 \pm 0.004$ |
| $1.635 \pm 0.084$ | $2.222 \pm 0.035$ | $0.031 \pm 0.005$ |

measurements in the axial direction with a single laser beam pair satisfy completely the requirements for volume fraction measurement. Therefore, the velocity and volume fraction measurements were done sequentially.

The fiber optic LDA probe was mounted on a special traversing mechanism, which allowed full probe positioning in all three orthogonal directions with an accuracy of $\pm 1\,\mu$m. The nearest position of the measuring volume to the wall was established by moving it until the FEP pipe started interfering with the measurement. The switch from the typical velocity burst signal, measured on the oscilloscope, to a distorted signal due to the wall interference, was clearly evident. In this way we were able to establish the position of the measuring volume by knowing the dimensions of the FEP pipe. The closest point of the measuring volume to the pipe wall, without significant wall interference, was approximately at $r/R = 0.985$ (i.e. $r = 15.1$ mm), where $R$ is the pipe radius.

A single-beam traversing $\gamma$-ray densitometer was used as a reference for the volume fraction measurements. As shown in figures 1 and 2, a shielded container with a 5 Ci $^{137}$Cs source was placed just below the test section. The attenuated collimated $\gamma$-ray beam was measured using an NaI crystal photomultiplier, which was connected in turn to a Canberra multichannel analyzer (Series 20). In gas/liquid systems the chordal-average gas volume fraction, $\bar{\epsilon}_G$, measured with a single-beam $\gamma$-ray densitometer, is (Schrock 1969):

$$\bar{\epsilon}_G = \frac{\ln\left(\frac{I}{I_L}\right)}{\ln\left(\frac{I_G}{I_L}\right)}, \qquad [7]$$

where $I$ is the intensity of the $\gamma$-beam through the two-phase mixture, $I_G$ is the intensity of the beam with the gas phase only and $I_L$ is the intensity of the beam with the liquid phase only. This equation cannot be applied directly to the solid phase appearing in the form of spheres. Even at the highest possible concentration the spherical solid particles have small gaps between them; indeed, the maximum achievable volume fraction with uniform spheres is 74.05%. As derived in appendix A, the effect of this bed porosity is accounted for in the following equation:

$$\bar{\epsilon}_S = \bar{\epsilon}_{S0} \frac{\ln\left(\frac{I}{I_L}\right)}{\ln\left(\frac{I_{SL}}{I_L}\right)}, \qquad [8]$$

where $\bar{\epsilon}_{S0}$ is the reference chordal volume fraction at the maximum particle concentration and $I_{SL}$ is the intensity of the beam when $\bar{\epsilon}_S = \bar{\epsilon}_{S0}$, liquid being the continuous phase. The reference chordal-average volume fraction can be calculated as

$$\bar{\epsilon}_{S0} = 1 + \frac{\ln\left(\frac{I_{SL}}{I_{SG}}\right)}{(\mu_L - \mu_G)L}, \qquad [9]$$

where $I_{SG}$ is the intensity of the beam at $\bar{\epsilon}_S = \bar{\epsilon}_{S0}$ and gas is the continuous phase. These equations and an estimation of the related errors are given in appendix A.

It is important to note that $I_{SL}$ and $I_{SG}$ must be measured for the same particle configuration. This was achieved by first filling an empty pipe with particles and measuring the intensity of the beam, $I_{SG}$, at $\bar{\epsilon}_S = \bar{\epsilon}_{S0}$, with air filling the gaps between the particles. A mesh at the bottom of the pipe held the particles in place. Next, water was poured into the pipe. This procedure was carried out with great care in order to maintain the same particle configuration in both cases. The intensity of the beam, $I_{SL}$, was measured again at $\bar{\epsilon}_S = \bar{\epsilon}_{S0}$, with the liquid filling the gaps. The whole measurement procedure was repeated several times. All the results were within the margin of error estimated for this experiment.

### *2.1. Separation of Large Particles from Seeding*

The purpose of the present work was to measure the phase distributions of large spherical particles, approximately 2 mm in diameter. In addition to the large particles, there are always

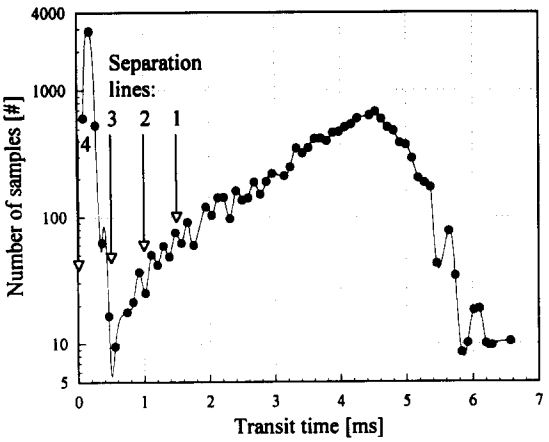


Figure 4. Measured transit time distribution.

present tiny impurities or seeding, carried by the liquid phase. They are also detected by the LDA system and their transient time contributes to the particle volume fraction. Since an LDA system is sensitive to particle sizes down to 1 $\mu$m, it is difficult to get rid of this effect. However, filtration helps to reduce the overall amount and mean size of the unwanted small particles. Figure 4 shows a typical transit time distribution. The peak on the left-hand side is due to the seeding, while the peak on the right-hand side is due to the large particles.

It can be noticed that there is a large difference in the measured transient times of each particle group, which is due to the size difference. Thus, separation can be based on the difference between the large particle and seeding transit times. In the case where the difference in sizes is not so large, other methods should be applied. Qiu *et al.* (1991) developed a method for distinguishing dispersed particles ($D_p = 45.5$ $\mu$m) from the seeding ($D_p = 6$ $\mu$m) using a phase-Doppler anemometer (PDA). For both the seeding and the particles they used glass beads, which have a very smooth surface. In the present case, however, the high surface porosity of the large particles distorted the PDA signal too much and made the use of this method inappropriate.

Figure 4 shows four separation lines, which could be used to separate the two particle groups. All the particles on the right-hand side of each separation line were used to calculate the large particle volume fraction. The results are shown in table 5, where $t_{s,i}$ stands for the transit time of the $i$th separation line and $\epsilon_i$ is the corresponding volume fraction. Separation line 3, which is placed at the minimum between the two peaks, is the one which would be normally used to separate particles. From figure 4 it is evident that such a separation might reject the contribution of large particles with small transit times (i.e. those large particles passing through the edge of the measurement volume). Fortunately, it was shown that this error is negligible.

From Table 5, it follows that the difference between the values obtained using separation lines 2 and 3 is about 1%. This difference is larger than that which would be obtained by extrapolating the large particle distribution towards zero and calculating the contribution to the volume fraction under the extrapolation line. A similar conclusion is reached for the seeding. Its contribution to the measured volume fraction is insignificant. Therefore, the particle separation using line 3 seems to be justified, resulting in the smallest error.

Table 5. Volume fraction as a function of the transit time separation

| $i$ | $t_{s,i}$ [ms] | $\epsilon_i$ [%] | $\frac{\epsilon_i}{\epsilon_3}$ |
|---|---|---|---|
| 1 | 1.50 | 0.642 | 0.97 |
| 2 | 1.00 | 0.657 | 0.99 |
| 3 | 0.58 | 0.663 | 1.00 |
| 4 | 0.00 | 0.853 | 1.29 |

### 2.2. Corrections Due to the Finite Size of the LDA Measurement Volume

A correction can be done if the size and shape of the measurement volume are known. Saffman (1987) proposed the use of the average burst length to determine the size of the measurement volume. This is valid when the particles are smaller than the measurement volume. Unfortunately, the same method cannot be applied here, since the large particles are several times larger than the measurement volume. Furthermore, the large particles interrupt the beams between the measurement point and the LDA transmitter/receiver, distorting the measured distribution of the transit times. The other option is to use a reference measurement to estimate the correction needed for the integration, as done by Sommerfeld & Qiu (1991). Their method, based on the use of a PDA, consisted of correcting the measured mass flux due to the uncertainties in the determination of the measurement volume by using a global mass balance. This was possible, since they used very small particles ($D_p = 45.5\ \mu m$) which did not cause beam interruptions.

We followed a similar approach. A single-beam $\gamma$-ray densitometer was used to measure the chordal-average volume fraction at the pipe centerline. This result was used as the calibration for a correction factor, $C$, which accounts for the uncertainties in the calculation of the measurement volume. It was determined in the following way: all the values in the measured volume fraction profile were multiplied by a guessed $C$, then corrected for the beam interruptions (using the method presented in the next section), and finally integrated over the centerline chord. If this value equaled that measured by the $\gamma$-ray densitometer, the procedure was ended. Otherwise, a new $C$ was guessed and the same procedure repeated until the convergence was achieved. Note that by changing the properties of the large particles, the calibration procedure must be repeated.

This method assumes that $C$ is not a function of the radial position. This is not self-evident, since there might be some spatial differences in, for example, the transmissivity of the medium from point to point. Thus, let us next consider the experimental results which justify the assumption of a constant $C$.

The LDA probe volume is normally defined as the region in space within which the light intensity is at least $e^{-2}$ of its peak value at the crossing of the two Gaussian-shaped laser beams. However, the true measurement volume is not necessarily bounded by the $e^{-2}$ contour. In fact, the measurement volume is just the region from where the system actually detects the scattered light from the particles. Besides the beam intensity, this region depends on the electronic gain, the transmissivity of the medium and the size and shape of the particles. The scattered intensity is proportional to $D_p^2$ (Saffman 1987), where $D_p$ is the particle diameter. The measurement volume for the large particles is therefore larger than for the seeding. Hence, the actual measurement volume should be bounded by $e^{-k}$ instead of the $e^{-2}$ contour, where $k > 0$. In the case of the large particles, $k$ should be $k \geqslant 2$. The light intensity distribution, at the crossover of two Gaussian beams of equal power is proportional to (Brayton 1974):

$$\langle \mathbf{S} \rangle \sim \frac{P}{r_f^2} \exp\left\{ -\frac{2}{r_f^2} [x^2 \cos\theta + y^2 + z^2 \sin\theta] \right\} \cos\left( \frac{2\pi y}{\delta} \right), \qquad [10]$$

where $P$ is the total power contained in the beam, $r_f$ is the radius of the focused Gaussian beam at the $e^{-2}$ intensity point, $x$, $y$ and $z$ are the coordinates of the measurement volume, $\theta$ is the half-angle of the beam intersection, $\delta$ is the fringe spacing and $\langle \mathbf{S} \rangle$ is the amplitude of the time-averaged Poynting vector, defined as

$$\langle \mathbf{S} \rangle = \tfrac{1}{2} \mathrm{Re}(\mathbf{E} \times \mathbf{H}^*). \qquad [11]$$

The electric field vector $\mathbf{E}$ and complex conjugate of the magnetic field vector $\mathbf{H}^*$ can be decomposed as

$$\mathbf{E} = \mathbf{E}_1 + \mathbf{E}_2 \qquad [12]$$

and

$$\mathbf{H}^* = \mathbf{H}_1^* + \mathbf{H}_2^*, \qquad [13]$$

where the subscripts 1 and 2 stand for the first and second beam, respectively. The radius of the focused Gaussian beam at the $e^{-2}$ intensity point is defined as (Kogelnik 1965; Farmer & Brayton 1971):

$$r_f = \frac{2f\lambda}{\pi E d}, \quad [14]$$

where $f$ is the lens focal length, $\lambda$ is the wavelength of the laser beam, $E$ is the expansion ratio and $d$ is the diameter of the unfocused beam at the $e^{-2}$ intensity point. The intensity is reduced to $e^{-k}$ of its peak value when the argument of the exponent in [10] equals $-k$ (Brayton *et al.* 1973). All the points located at the $e^{-k}$ contour form an ellipsoid with parameters $a$, $b$ and $c$. Thus,

$$a^2 \cos\theta + b^2 + c^2 \sin\theta = k\frac{2}{r_f^2}; \quad [15]$$

hence

$$2a = \frac{\sqrt{2k}r_f}{\cos\theta}, \quad [16]$$

$$2b = \frac{\sqrt{2k}r_f}{\sin\theta} \quad [17]$$

and

$$2c = \sqrt{2k}r_f. \quad [18]$$

The angle $\theta$ is very small, in general. Thus, $\cos\theta$ approximately equals unity with $a \cong c$, $b \gg a$ and $b \gg c$. Note that the size of parameters $a$, $b$ and $c$ depends on the scattered light intensity. The parameters affecting the scattered intensity are the size of the particles, the transmissivity of the medium etc.

Next, the correction due to the integration in the measurement volume can be done. The ratio between the volume fraction measured at the ideal point to the volume fraction actually measured in the measurment volume is defined as the correction coefficient,

$$C(r_i) = \frac{\sum_{j=1}^{N_{MP}} \epsilon_j(r_i)}{\sum_{j=1}^{N_{MV}} \epsilon_j(r_i)}, \quad [19]$$

where $\epsilon_j(r_i)$ is the contribution of the $j$th particle to the volume fraction measured at $r_i$, $N_{MP}$ is the number of particles which interact with the ideal measurement point (MP) during the measurement time, $T$, and $N_{MV}$ is the number of particles interacting with the actual measurement volume (MV) with its center at $r_i$.

Figure 5 is used to illustrate the contribution of a single spherical particle to the volume fraction at the location $r_i$. The particle's transit time, $t_j$ (i.e. the time during which the particle is in contact with the MP), is equal to the chordal length of the particle, which passed the ideal measurement point, divided by the particle's velocity, $u_{p,j}$:

$$t_j = \frac{2\sqrt{R_{p,j}^2 - r^2}}{u_{p,j}}, \quad [20]$$

where, $R_{p,j}$ is the radius of the $j$th particle. Its contribution to the volume fraction at the location $r_i$ equals the ratio between its transit time, $t_j$, and the total time of measurement, $T$:

$$\epsilon_j(r_i) = \frac{t_j}{T} = \frac{2\sqrt{R_{p,j}^2 - r^2}}{u_{p,j}}\frac{1}{T}. \quad [21]$$

By assuming that all the particles have the same size, $\bar{R}_p$, each particle within distance $\bar{R}_p$ from the location $r_i$ contribute to the volume fraction. Moreover, it can be assumed that all the

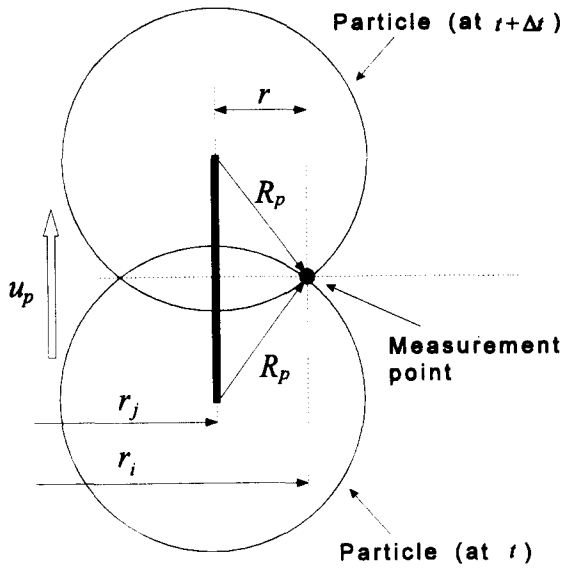


Figure 5. Single particle contribution to the volume fraction measurement at the measurement point (MP) location $r_i$.

particles move only in the axial direction with the same velocity $\bar{u}_p$. Hence, the volume fraction at $r_i$ equals

$$\sum_{j=1}^{N_{MP}} \epsilon_j(r_i) = \int_0^{2\pi} \int_0^{\bar{R}_p} n''(r_j) \frac{2\sqrt{\bar{R}_p^2 - r^2}}{\bar{u}_p T} r \, dr \, d\psi, \quad [22]$$

where $\psi$ is the angle between $r_i$ and $r$ in the plane perpendicular to the particle motion and $n''(r_j)$ is the concentration of particles per unit area at $r_j$. The location of the $j$th particle's center, $r_j$, can be expressed using the radial position of the measurement point, $r_i$, and the distance between the particle center and the measurement point, $r$:

$$r_j = \sqrt{r_i^2 + r^2 - 2r_i r \cos\psi}\,. \quad [23]$$

If $n''$ depends only on the radial position in the pipe, $r_i$, which is usually the case, it can be expanded around $r_i$ and used in [22]:

$$\sum_{j=1}^{N_{MP}} \epsilon_j(r_i) = \int_0^{2\pi} \int_0^{\bar{R}_p} \left[ n''(r_i) + r \cos\psi' \frac{\partial n''(r_i)}{\partial r_i} \right] \frac{2\sqrt{\bar{R}_p^2 - r^2}}{\bar{u}_p T} r \, dr \, d\psi'$$

$$= \frac{4}{3} \pi \bar{R}_p^3 \frac{n''(r_i)}{\bar{u}_p T}, \quad [24]$$

where $\psi' = \psi - \pi$. This equation is valid as long as the first-order Taylor expansion is appropriate (i.e. where the spatial changes in the volume fraction can be linearized over the integration region in the above integral). Notice that the single particle contribution to the volume fraction equals the volume of the region from where the particles act on the MP times $n''(r_i)/\bar{u}_p T$.

The expression for the measured volume fraction in the MV can be derived in the same way. figure 6(b) depicts how a single particle interacts with the measurement volume. The transit time, $t_j$, of the $j$th particle equals the distance traveled by the particle, while in contact with the measurement volume, divided by its velocity, $u_{p,j}$. In the actual case only a portion of the particle's frontal area may contribute to the detected back scattered light. This region is shown in figure 6(a). It is assumed that the radius of this region, $R_p'$, is linearly proportional to the particle radius, $R_p$. Thus,

$$R_p' = FR_p \quad (0 \leqslant F \leqslant 1). \quad [25]$$

The coefficient $F$ might vary from particle to particle, and is mainly dependent on the surface roughness at the particle's far ends.

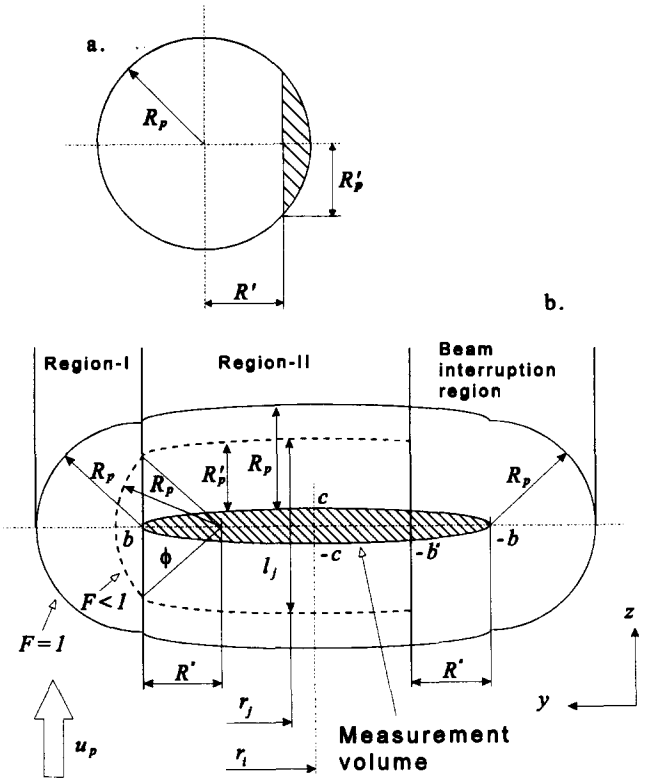


Figure 6. Single particle contribution to the volume fraction measurement at the measurement volume (MV) location $r_i$.

Figure 6(b) shows two possible contours, one for $F = 1$ and the second for $F < 1$. The general case with $F \leqslant 1$ is considered in the derivation of the measured volume fraction in the MV. The contour represents the interaction region around the measurement volume, from which each particle with its center in it interacts with the measurement volume.

Let us consider the $j$th particle with its center moving at $r_j - R'_j$. It travels the distance $l_j$ between the two contour ends at $r_j$ (contour at $F < 1$), while in contact with the measurement volume. The parameters shown in figures 6(a) and (b) are defined as

$$R'_j = R_{p,j} \sin\left(\arccos \frac{R'_{p,j}}{R_{p,j}}\right) = R_{p,j} \sin(\arccos F_j), \qquad [26]$$

$$b'_j = b - (R_{p,j} - R'_j) \qquad [27]$$

and

$$\phi_j = \arctan \frac{R'_{p,j}}{R_{p,j}} = \arctan F_j. \qquad [28]$$

After specifying these parameters for the general case, let us assume that all the particles have the same size, $\bar{R}_p$, move with the same velocity, $\bar{u}_p$, and have the same scattering coefficient, $F$. Based on [24], the measured volume fraction can be expressed as

$$\sum_{j=1}^{N_{MP}} \epsilon_j(r_i) = (V_I + V_{II}) \frac{n''(r_i)}{\bar{u}_p T}. \qquad [29]$$

The interaction volume has been divided into two regions for calculation convenience. Thus,

$$V_I = \tfrac{1}{3}\pi(\bar{R}_p - R')(2\bar{R}_p + R') \qquad [30]$$

$$V_{II} = \pi \int_{-b'}^{b} x^2(y)\,dy = \pi \int_{-b'}^{b} \left(\bar{R}_p + a\sqrt{1-\frac{y^2}{b^2}}\right)^2 dy$$

$$= \pi\left[(\bar{R}_p^2 + a^2)(b^2 - b'^2) + \bar{R}_p^2 \frac{b'}{b}\sqrt{b^2 - b'^2} + \bar{R}_p ab\left(\frac{\pi}{2} + \arcsin\frac{b'}{b}\right) - \frac{a^2}{3b^2}(b^3 + b'^3)\right]; \quad [31]$$

$V_I$ and $V_{II}$ are the volumes of the two interaction regions. Each particle falling in the beam interruption region [figure 6(b)] is presumed to interrupt the laser beam (or beams) instead of being detected. The interruption region is on the side oriented towards the transmitting/receiving optics. Finally, the correction coefficient $C$ equals

$$C = \frac{\frac{4}{3}\pi\bar{R}_p^3}{(V_I + V_{II})}. \quad [32]$$

The correction coefficient, $C$, as a function of the axial dimension of the measurement volume, $a$, has been calculated for the parameters shown in table 1 and $D_p = 2.32$ mm for various values of the coefficient $F$. Note that the measurement volume parameters $a$, $b$ and $c$ are particle-size-dependent. The results are shown in figure 7. The dimension, $b$, of the measurement volume has been calculated by choosing $a$ first, $k$ was obtained from [16], and finally, by using [17], $b$ was calculated. These parameters were used in [30]–[32] to calculate $C$. In order to obtain the volume fraction within 10% accuracy, $C$ should not vary more than $\pm 0.01$ mm in the present case (figure 7).

The size of the measurement volume decisively affects the distribution of the particle chordal lengths given by the product of the $j$th particle's transit time and its velocity:

$$l_j = t_j u_{p,j}. \quad [33]$$

The distance $l_j$ equals the distance traveled by the particle at the radial position $r_j - R_j'$, while in contact with the measurement volume [figure 6(b)]. The measured distribution of particle chordal lengths, $l_j$, for 10,000 collected samples is shown in figure 8 as curve a. The distribution was measured near the pipe wall, at $x = 0$ mm and $y = -12$ mm, in order to minimize the beam interruptions as much as possible.

The model presented herein was used to predict the measured distribution for $l_j$. Particles were generated randomly in the $x$–$y$ plane in the region where they could intersect the measurement volume. The particle size distribution which was used is shown in figure 3. The chordal length, $l_j$, is a function of the position, particle size, the parameter $a$ and the coefficient $F$. In region-I,

$$l_j = 2\sqrt{R_{p,j}^2 - (x^2 + y^2)}. \quad [34]$$

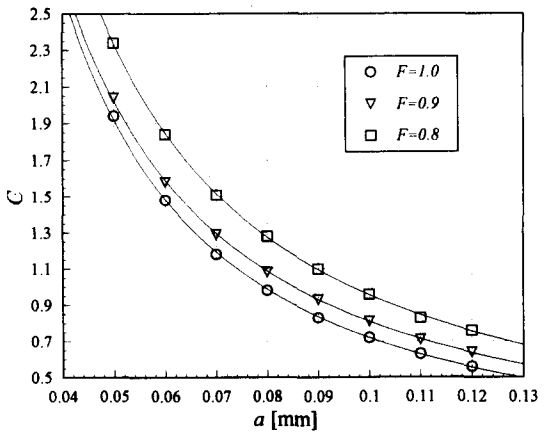


Figure 7. Correction coefficient, $C$, as a function of the parameters $a$ and $F$.

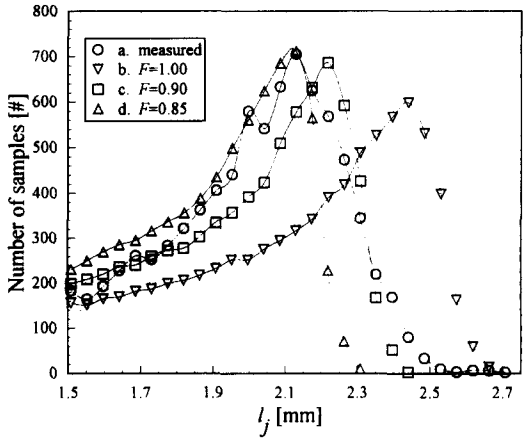


Figure 8. Measured and generated particle chordal length distributions.

Similarly, in region-II,

$$l_j = 2\sqrt{\left[R_j + a\left(1 + \frac{y^2}{b^2}\right)\right]^2 - x^2}. \quad [35]$$

The other parameters used in this simulation are given in table 1.

The parameters $a$ and $F$ were estimated by fitting the measured distribution, obtained at $x = 0$ mm and $y = -12$ mm (figure 8, curve a). The measured distribution had its peak at about 2.10 mm, which is less than the mean particle size. This confirms that only part of the particle's frontal area scatters the light back to the receiving optics. Hence, $F < 1$ in the actual case. Figure 8 shows the comparison between the measured (curve a) and the generated distributions. These curves were generated by keeping constant the measurement volume parameter $a = 0.1$ mm ($b = 1.18$ mm), while changing $F$. Figure 8 shows the simulation at $F = 1$, 0.9 and 0.85 (curves b, c and d, respectively). Curve c is the one which gives the best fit to the measured distribution. Thus, the parameters $a = 0.1$ mm and $F = 0.9$ were used in the following analysis.

Comparing the generated distributions with the measured one in figure 8 leads to the conclusion that the simulations gave qualitatively good results, even if they are not good enough to estimate the measurement volume size with a desired accuracy. It seems that the model has captured the physics of the particle interaction with the measurement volume quite well.

Next, the measured distributions at three different point along the $x$-axis ($x = 0$, 6 and 10 mm) were compared with that measured at $x = 0$ mm and $y = -12$ mm. The comparison is shown in figure 9(a). It can be noticed that the peaks and end points of the measured distributions are all at the same location. They have almost identical shapes. The main difference is in the more flattened distributions for the data obtained at $y = 0$ mm. This is caused by the greater effect of beam interruptions at the pipe's centerline, which tends to decrease the average length of the transit time.

As stated before, $C$ should not vary more than 10% in order to obtain the measured volume fraction within 10%. Therefore, the measurement volume parameter, $a$, should not vary more than $\pm 0.01$ mm (figure 7). The parameters affecting its size are primarily the transmissivity of the medium, the particle size and the LDA system setup. Three distributions were generated by the model presented above at $F = 0.9$ and $a = 0.11$, 0.1 and 0.09, and are shown in figure 9(b). They have different shapes from the measured distributions in figure 9(a); whereas the measured distributions have almost identical shapes. Since they were measured at different radial positions, it can be concluded that their measurement volume size was not position-dependent. Thus, taking the correction coefficient, $C$, to be constant is justified.

The difference in the location of the peaks and the shapes of the measured transit time distributions at different radial positions represents a good test for the use of the constant correction coefficient, $C$. The negligible difference justifies the assumption that $C$ does not vary with the radial position.

### 2.3. *Correction for Beam Interruptions*

Marié & Lance (1984) measured the laser beam interruption factor in bubbly flows for different channel widths and vapor volume fractions. They showed that this effect is far from negligible. Yu

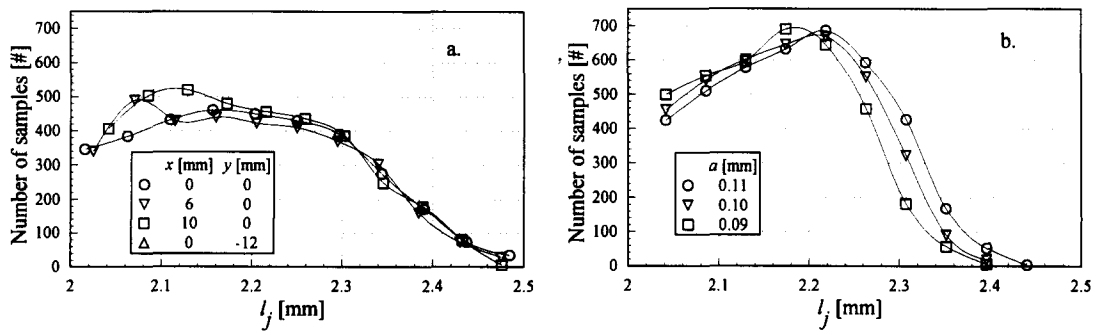


Figure 9. Estimation of the change in measurement volume size: (a) measured and (b) generated particle chordal length distributions.

& Varty (1988) calculated it for bubbly flow in the case where the transmitting and receiving optics were separated. They neglected the possibility of having two bubbles interrupting the same beam simultaneously. This effect might be negligible at low volume fractions, but at high volume fractions it tends to overpredict the interruptions. Let us now consider an analysis which takes into account the possibility of having many particles interrupting the laser beam at the same instant.

The measure of the interruptions is defined as the ratio between the time, $t$, during which the laser beam between the transmitter/receiver and measurement point was interrupted, and the entire measurement time, $T$. This ratio is denoted by $A$:

$$A(r) = \frac{t(r)}{T(r)}. \qquad [36]$$

We may assume that $A$ is a function of the volume fraction and its distribution:

$$A(r) = f(\epsilon, r). \qquad [37]$$

In the first step, $A$ is calculated for the case shown in figure 10, assuming that the volume fraction $\epsilon_i$ in subchannel $r_i$ is independent of the volume fraction in other subchannels. This is the case for particles moving in confined subchannels, where they are not allowed to move between the subchannels. Let an observer be placed right on the interface between the channels at $r_1$ and $r_2$, and let this observer measure the time fraction during which the laser beam is interrupted. Since the particle motion is confined to a single subchannel, each particle contributes to the volume fraction in that subchannel only. Because of this, an observer placed on the interface between the two subchannels at $r_1$ and $r_2$ would measure

$$A(r_1) = \epsilon_1. \qquad [38]$$

Similarly, on the interface between the subchannels at $r_2$ and $r_3$,

$$A(r_2) = \epsilon_2 + (1 - \epsilon_2)\epsilon_1. \qquad [39]$$

If the observer is placed now at the end of the subchannel at $r_5$, the beam interruption measured would be

$$A(r_5) = \epsilon_5 + (1 - \epsilon_5)[[\epsilon_4 + (1 - \epsilon_4)\{\epsilon_3 + (1 - \epsilon_3)[\epsilon_2 + (1 - \epsilon_2)\epsilon_1]\}]], \qquad [40]$$

which can be rearranged as

$$A(r_5) = \epsilon_5 + (1 - \epsilon_5)\epsilon_4 + (1 - \epsilon_5)(1 - \epsilon_4)\epsilon_3 + (1 - \epsilon_5)(1 - \epsilon_4)(1 - \epsilon_3)\epsilon_2 + (1 - \epsilon_5)(1 - \epsilon_4)(1 - \epsilon_3)(1 - \epsilon_2)\epsilon_1 \qquad [41]$$

or

$$A(r_5) = \sum_{i=1}^{5} \epsilon_i \prod_{k=i+1}^{5} (1 - \epsilon_k). \qquad [42]$$

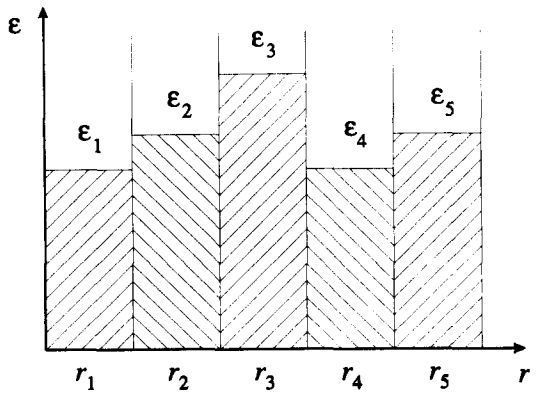


Figure 10. Volume fraction distribution for the particle flow in subchannels.

The extension to $N$ subchannels is easily obtained as

$$A(r_N) = \sum_{i=1}^{N} \epsilon_i \prod_{k=i+1}^{N} (1 - \epsilon_k). \quad [43]$$

In the actual case, however, the volume fractions in the subchannels are interdependent. The particle can contribute to the volume fraction in two subchannels simultaneously. As a result [43] is no longer valid.

Let us now assume that the particles move in the axial direction only. In that case, the particle contribution to the beam interruption is the largest in the subchannel which includes its center. Hence, the subchannels can be made virtually independent by considering only the portion of the volume fraction due to the particles whose centers fall in that subchannel:

$$\epsilon_i' = \epsilon_i K(r_i, \Delta r), \quad [44]$$

where $K(r_i, \Delta r)$ equals the fraction of the volume in the subchannel at $r_i$, having width $\Delta r$, which is due to the particles having their centers in that subchannel. It is defined as

$$K(r_i, \Delta r) = \frac{\sum_{j=1}^{N_{r_i}} \epsilon_j(r_i)}{\sum_{j=1}^{N_{r_i,\text{all}}} \epsilon_j(r_i)}, \quad [45]$$

where $N_{r_i}$ is the number of particles with centers in the channel at $r_i$ and $N_{r_i,\text{all}}$ is the number of all particles contributing to the volume fraction at the location $r_i$. Equation [43] can be used now in the modified form

$$A(r_N) = \sum_{i=1}^{N} \epsilon_i' \prod_{k=i+1}^{N} (1 - \epsilon_k') \quad [46]$$

or, by [44],

$$A(r_N) = \sum_{i=1}^{N} \epsilon_i K(r_i, \Delta r) \prod_{k=i+1}^{N} [1 - \epsilon_k K(r_k, \Delta r)]. \quad [47]$$

Equation [47] gives the interruption coefficient for a single laser beam.

In order to calculate $A$ from [47], the coefficient $K(r_i, \Delta r)$ must be found. The following assumptions were made in its calculation:

(1) The laser beam can be approximated by a line (i.e. the laser beam's cross section is negligible).
(2) All the particles have the same spherical shape and size.
(3) The spatial changes in the particle concentration, $n''$, can be linearized in the immediate vicinity of the particle.
(4) All the particles at $r_i$ are traveling with the same velocity, $\bar{u}_p$.

The volume fraction at point $r_i$ is, according to [24],

$$\epsilon_i = \sum_{j=1}^{N_{r_i,\text{all}}} \epsilon_j(r_i) = \frac{4}{3} \pi \bar{R}_p^3 \frac{n''(r_i)}{\bar{u}_p T}. \quad [48]$$

The subchannel width $\Delta r$ is chosen such that $\Delta r \ll \bar{R}_p$. Equation [24] leads to the following result for the portion of the volume fraction in the subchannel at $r_i$ due to the particles with their centers in that subchannel:

$$\sum_{j=1}^{N_{r_i}} \epsilon_j(r_i) = \pi \bar{R}_p^2 \Delta r \frac{n''(r_i)}{\bar{u}_p T}. \quad [49]$$

By using [45], [48] and [49], coefficient $K$ becomes

$$K(r_i, \Delta r) = K(\Delta r) = \frac{3\Delta r}{4\bar{R}_p}. \quad [50]$$

Combining [47] and [50] gives the fraction of the measurement time, $T$, during which the single beam is interrupted:

$$A^1(r_N) = \sum_{i=1}^{N} \epsilon_i \frac{3\Delta r}{4\bar{R}_p} \prod_{k=i+1}^{N} \left(1 - \epsilon_k \frac{3\Delta r}{4\bar{R}_p}\right). \quad [51]$$

Since the LDA system has two beams, the interruption coefficient for the beam pair at $r_N$ is

$$A(r_N) = A^1(r_N) + A^2(r_N) - A^1(r_N)A^2(r_N). \quad [52]$$

This equation is valid if the interruptions of the two beams are independent (or exclusive) events, where $A^1$ and $A^2$ are the beam interruption fractions for the first and the second beam, respectively. However, near the measurement volume $A^1$ and $A^2$ are not independent. At the beam crossover the two beams lie close together, allowing some particles to interrupt both beams simultaneously. The coefficient $K$ for the second beam should thus be modified in order to consider this effect.

Figure 11 shows the shaded region from where the particles with centers within it interrupt both beams at the same time. Let the contribution of those particles be counted in the interruption fraction of the first beam. Therefore, the coefficient $K$ for the second beam is modified as

$$K_2(\Delta r) = \frac{\pi \bar{R}_p^2 \Delta r - (\beta - \sin\beta)\bar{R}_p^2 \Delta r}{\frac{4}{3}\pi \bar{R}_p^3} = \frac{3\,\Delta r}{4\bar{R}_p} \frac{\pi - (\beta - \sin\beta)}{\pi}, \quad \text{for } \frac{l'}{2} < \bar{R}_p \quad [53]$$

and

$$K_2(\Delta r) = K_1(\Delta r), \quad \text{for } \frac{l'}{2} \geqslant \bar{R}_p, \quad [54]$$

where $(\beta - \sin\beta)\bar{R}_p^2 \Delta r$ is equal to the volume of the shaded area in figure 11. The other parameters in [53] are

$$l' = (s - \Delta s)\tan\theta \quad [55]$$

and

$$\beta = 2\arccos\left(\frac{l'}{2\bar{R}_p}\right). \quad [56]$$

Consecutively,

$$A^2(r_N) = \sum_{i=1}^{N} \epsilon_i \frac{3\,\Delta r}{4\bar{R}_p} \frac{[\pi - (\beta - \sin\beta)]}{\pi} \prod_{k=i+1}^{N} \left\{1 - \epsilon_k \frac{3\Delta r}{4\bar{R}_p} \frac{[\pi - (\beta - \sin\beta)]}{\pi}\right\}. \quad [57]$$

The interruption fraction of the two beams at the location $r_N$ is finally obtained from [52] using the appropriate values for $A^1$ and $A^2$, calculated by [51] and [57].

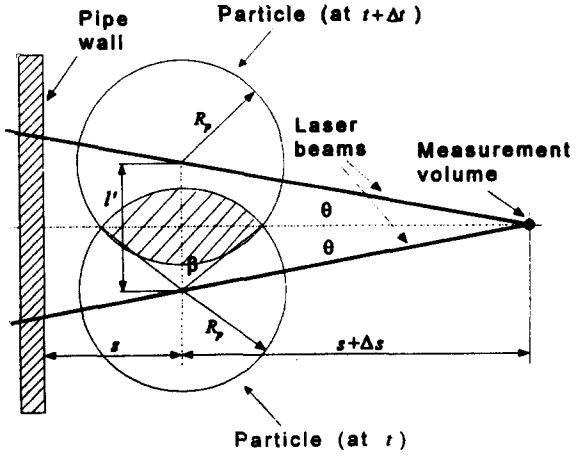


Figure 11. The region from where the particles interrupt both beams.

Table 6. Volume fraction results—ceramic particles

| $w$ [kg/s] | $\bar{\epsilon}_S$ [%] | $\bar{\epsilon}_{C,S}$ [%] | $\langle\epsilon_C\rangle$ [%] |
|---|---|---|---|
| 1.095 | $2.96 \pm 0.10$ | $2.83 \pm 0.18$ | $2.25 \pm 0.14$ |
| 1.469 | $3.30 \pm 0.15$ | $3.30 \pm 0.22$ | $2.23 \pm 0.13$ |
| 1.723 | $3.58 \pm 0.17$ | $3.75 \pm 0.25$ | $2.41 \pm 0.15$ |

Table 7. Volume fraction results—expanded polystyrene particles

| $w$ [kg/s] | $\bar{\epsilon}_S$ [%] | $\bar{\epsilon}_{C,S}$ [%] | $\langle\epsilon_C\rangle$ [%] |
|---|---|---|---|
| 1.060 | $1.31 \pm 0.16$ | $1.31 \pm 0.21$ | $1.40 \pm 0.21$ |
| 1.304 | $1.00 \pm 0.17$ | $1.17 \pm 0.18$ | $1.21 \pm 0.18$ |
| 1.635 | $0.90 \pm 0.17$ | $1.26 \pm 0.20$ | $1.25 \pm 0.19$ |

Factor $A$ should be evaluated over the entire laser beam section, $s$, stationed in the test section (see figure B1). The calculation of $s$ is done in the Cartesian coordinate system with its origin at the pipe centerline and the $z$-coordinate oriented in the pipe axial direction. The derivation is shown in appendix B. Once $A$ is obtained, the measured volume fraction, $\epsilon_m$, at position $r_N$ can be calculated from the actual volume fraction, $\epsilon$:

$$\epsilon_m(r_N) = \epsilon(r_N)[1 - A(r_N)]. \quad [58]$$

However, if $\epsilon_m$ is known instead, $\epsilon$ is

$$\epsilon(r_N) = \frac{\epsilon_m(r_N)}{[1 - A(r_N)]}. \quad [59]$$

The main error related to the coefficient $A$ is due to the deviation from the mean particle diameter. Therefore, the particle size distribution must be known in order to estimate the error of the correction procedure. The particle size distribution for the present case is shown in figure 3. It should be noted that the data correction procedure presented in this section is limited to dilute solid/liquid slurries. For high solid volume fractions, the required correction would be large and has not been verified in this study.

## 3. RESULTS AND DISCUSSION

### 3.1. Volume Fraction Data

The data for solid/fluid flow with ceramic particles are given in appendix C. They were taken for slurries at three different liquid flow rates. The corresponding $\gamma$-densitometer results for $\bar{\epsilon}_S$ are given in table 6.

The correction coefficient, $C$, has been calculated with the $\bar{\epsilon}_S$-value at $w = 1.469$ kg/s. The mean value of $C$ was obtained by fitting $\epsilon_S = 3.30\%$, using $D_p = 2.32$ mm in the interruption model. The error was estimated from the error in $\bar{\epsilon}_S$ and this error was related to the correction for the interruptions. At a constant global volume fraction, smaller particles interrupt the beams at a higher rate than the large ones. Since the model for the interruption correction is particle-size-

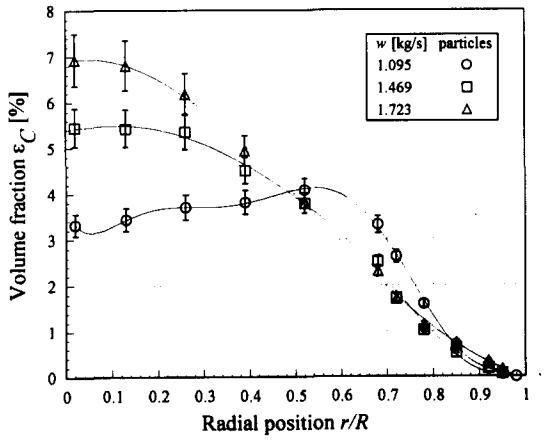


Figure 12. Corrected and uncorrected volume fraction profiles of the solid phase; solid/liquid flow with ceramic particles.

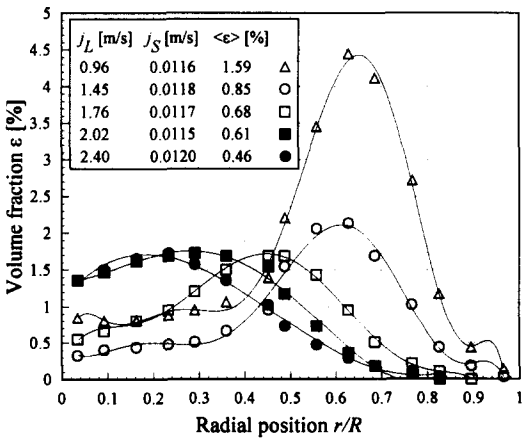


Figure 13. Volume fraction profiles of the solid phase (Sakaguchi *et al.* 1991).

dependent, $D_{p,min} = (2.32 - 0.07)$ mm and $\bar{\epsilon}_{S,min} = (3.30 - 0.15)\%$ were used to determine the lower margin of $C$, $C_{min}$. Similarly, larger particles with $D_{p,max} = (2.32 + 0.07)$mm and $\bar{\epsilon}_{S,max} = (3.30 + 0.15)\%$ were used to calculate $C_{max}$. The resultant $C$ and its standard deviation are:

$$C = 0.88 \pm 0.04. \quad [60]$$

This value has been used to correct the data. The estimation of the error in the corrected volume fraction, $\Delta\epsilon_C$, was based on the calculated error in the $\gamma$-ray measurements, $\Delta\epsilon_S$, and on the measured standard deviation of the particle size, the latter being the main source of error in the correction model:

$$\Delta\epsilon_C = \epsilon_{C,max} - \epsilon_{C,min}, \quad [61]$$

where $\epsilon_{C,max}$ was obtained using the upper margin of $C_{max} = 0.92$ and $\epsilon_{C,min}$ was obtained with the lower margin of $C_{min} = 0.88$.

Table 6 shows the chordal, $\bar{\epsilon}_{C,S}$, and global, $\langle\epsilon_C\rangle$, average volume fractions, both calculated from the corrected volume fraction profiles. The global volume fraction, $\langle\epsilon_C\rangle$, was obtained by integrating the corrected local volume fraction, $\epsilon_C$, over the pipe's cross section. The error in $\langle\epsilon_C\rangle$ was obtained from the error associated with $\epsilon_C$. Similarly, the chordal-average volume fraction, $\bar{\epsilon}_{C,S}$, was obtained by integrating the corrected volume fraction profiles over the chord at the pipe's centerline. Table 6 also gives the values of the chordal-average volume fraction, $\bar{\epsilon}_S$, measured by the single-beam $\gamma$-ray densitometer. It can be noted that the values for $\bar{\epsilon}_{C,S}$ and $\bar{\epsilon}_S$ are in good agreement for all the flow rates tested. To isolate the effect of the liquid velocity of the phase distribution, the data were obtained at an essentially constant global volume fraction, $\langle\epsilon_{C,S}\rangle$.

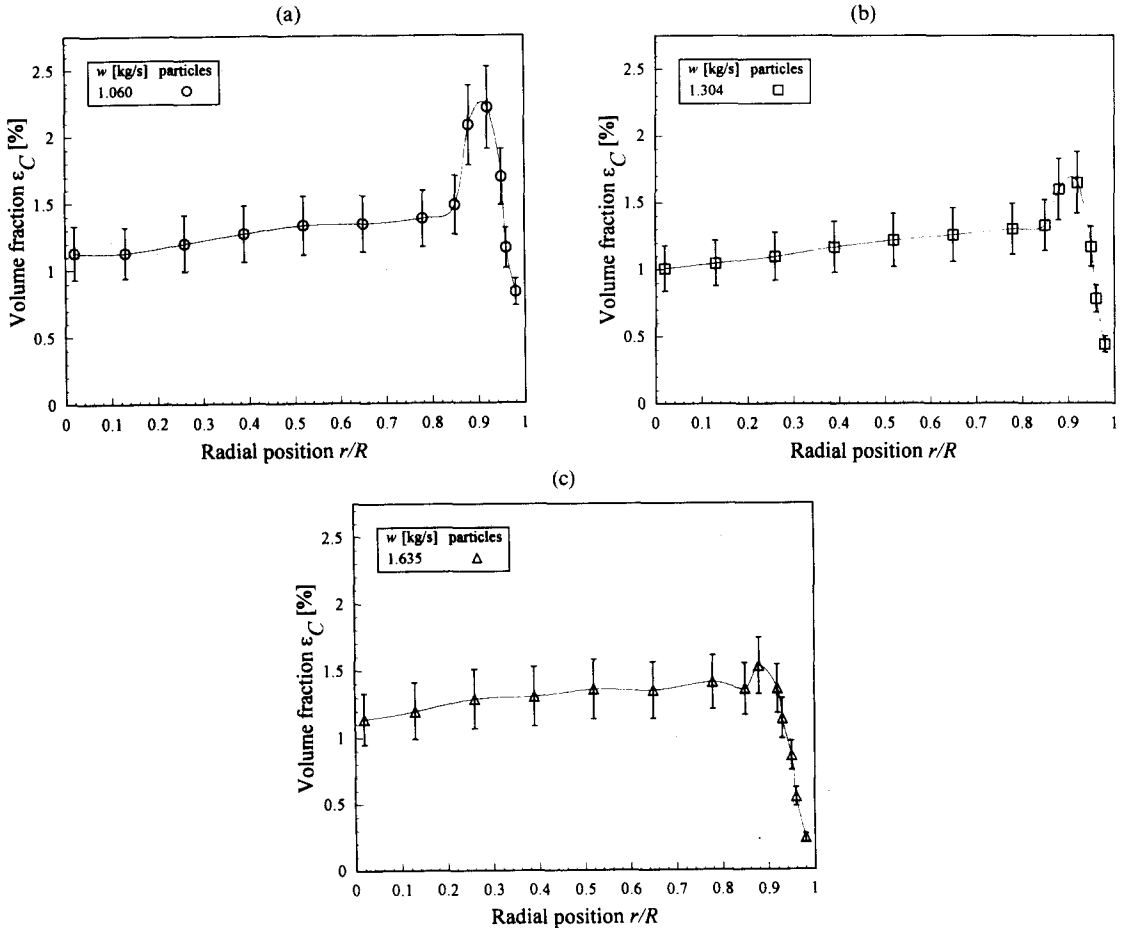


Figure 14. (a) Corrected volume fraction, $\epsilon_C$, profiles of the solid phase at $w = 1.060$ kg/s; solid/liquid flow with expanded polystyrene particles. (b) Corrected volume fraction, $\epsilon_C$, profiles of solid phase at $w = 1.304$ kg/s; solid/liquid flow with expanded polystyrene particles. (c) Corrected volume fraction, $\epsilon_C$, profiles of solid phase at $w = 1.635$ kg/s; solid/liquid flow with expanded polystyrene particles.

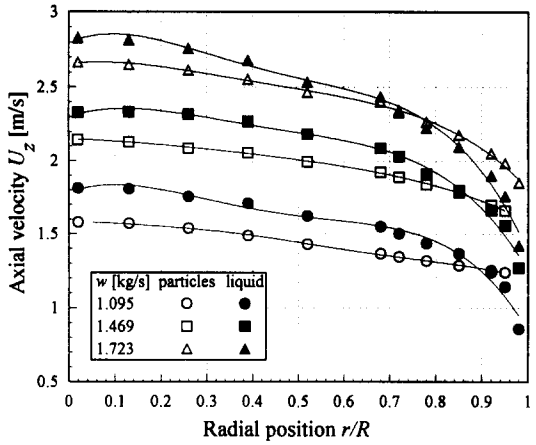


Figure 15. Velocity profiles for the solid and liquid phases; solid/liquid flow with ceramic particles.

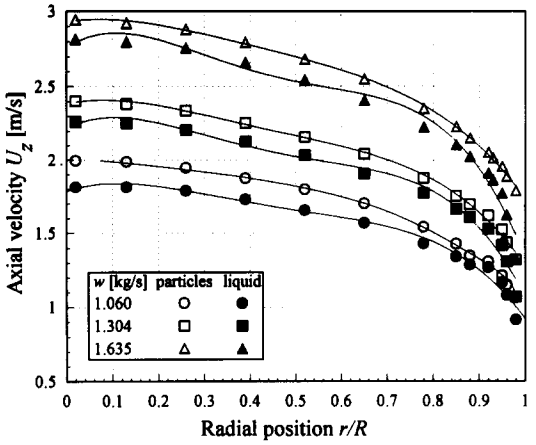


Figure 16. Velocity profiles for the solid and liquid phases; solid/liquid flow with expanded polystyrene particles.

The distributions of the corrected volume fraction profiles for the ceramic particles are shown in figure 12. Each point is plotted with its error bar in order to clarify the uncertainty in the measured results. A slight wall peak occurs at $w = 1.095$ kg/s; however, on increasing the liquid flow rate, the peak shifts towards the pipe's centerline (i.e. coring occurs). As can be seen in figure 13, similar trends were observed by Sakaguchi *et al.* (1991), however at different values of the superficial liquid velocities, $\langle j_L \rangle$, and volume fractions, $\langle \epsilon \rangle$. These differences are probably due to the fact that they used ceramic particles which were 4 mm in diameter, with a density equal to 2400 kg/m$^3$, and a pipe 30.8 mm in diameter.

It is also interesting to compare our results with the data of Lee & Durst (1982). In a similar experiment they observed that there was a particle-free region near the pipe walls in liquid flow for dispersed glass particles, 400 and 800 $\mu$m in diameter. The present data (figure 12) give essentially the same results. In any event, in all three studies, at the higher liquid velocities, there is a near-wall region, $0.8 < r/R < 1$, with almost no particles.

Data for the fluid flow with the expanded polystyrene particles are tabulated in appendix D. The correction factor which was obtained for $w = 1.060$ kg/s was $C = 0.80 \pm 0.10$. Table 7 shows the corrected chordal-average, $\bar{\epsilon}_{C,S}$, global volume fractions, $\langle \epsilon_C \rangle$, and the chordal-average solid fraction, $\bar{\epsilon}_S$, measured by the single beam $\gamma$-ray densitometer. Once again, the values $\bar{\epsilon}_{C,S}$ and $\bar{\epsilon}_S$ are in fairly good agreement.

The volume fraction distribution for the expanded polystyrene particles is shown in figures 14. A large wall peak is observed at the lowest liquid flow rate and flattens with the increase in the flow rate.

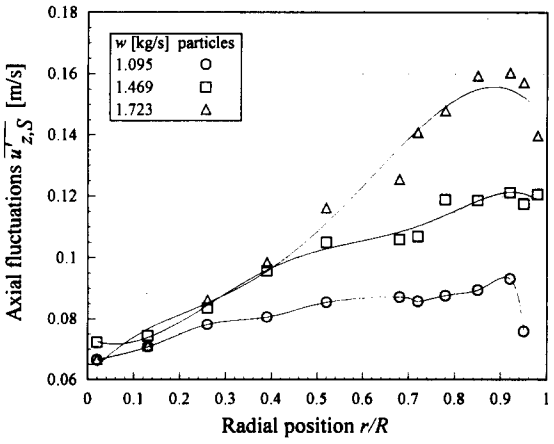


Figure 17. Axial turbulent fluctuations, $\overline{u'_{z,S}}$, for the solid phase; solid/liquid flow with ceramic particles.

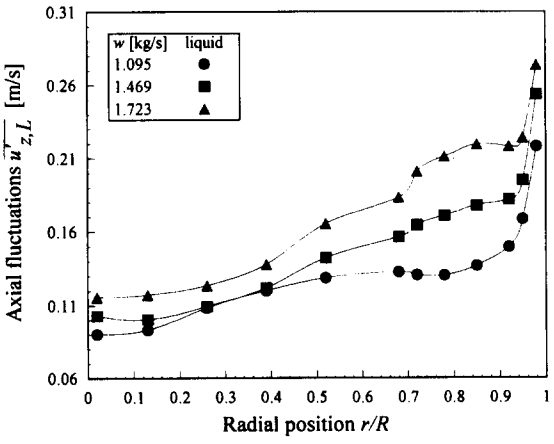


Figure 18. Axial turbulent fluctuations, $\overline{u'_{z,L}}$, for the liquid phase; solid/liquid flow with ceramic particles.

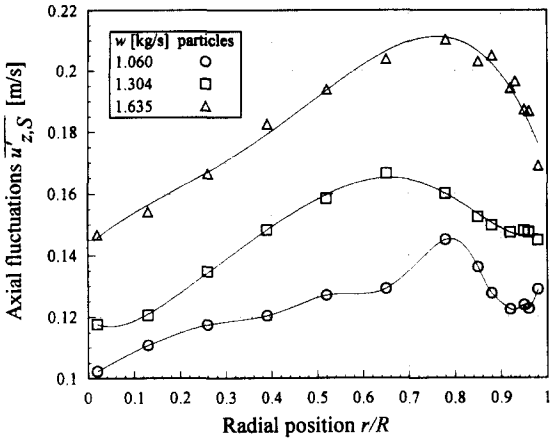


Figure 19. Axial turbulent fluctuations $\overline{u'_{z,S}}$ for the solid phase; solid/liquid flow with expanded polystyrene particles.

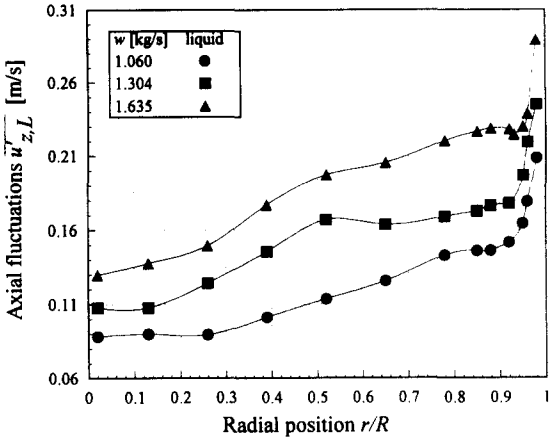


Figure 20. Axial turbulent fluctuations $\overline{u'_{z,L}}$ for the liquid phase; solid/liquid flow with expanded polystyrene particles.

### 3.2. Axial Velocity Data

The axial mean velocity, $U_z$, profiles for the ceramic particles and water are shown in Figure 15. As expected, the particles lag the liquid phase near the pipe's centerline, because of the negative buoyancy. The inverse effect is observed near the wall, i.e. the particles move faster than the liquid. At first sight, this seems controversial, however, the higher particle velocity near the wall is easily explained. The particles are large enough to be influenced not only by the slow moving liquid near the wall, but also by the liquid in the high-velocity region farther away from the wall. The net result is that the particles move faster than the liquid phase close to the wall, where the liquid velocity profile is steep.

It can be noticed that the higher the liquid flow rate, the lower the relative velocity between the particles and the liquid at the pipe's centerline. The opposite trend is observed in the volume fraction distribution, which tends to increase at the centerline with an increase in the flow rate. The observed reduction in the particle's relative velocity, $v_R$, is consistent with the increase in the volume fraction at the pipe centerline.

Figure 16 shows the velocity profiles for the expanded polystyrene particles. As expected, because of their positive buoyancy, the particles move faster than the liquid. Contrary to the ceramic particles, there is no switch in the sign of the light particle's relative velocity near the wall; however, at the lowest liquid flow rate, the relative velocity is reduced in the region near the wall.

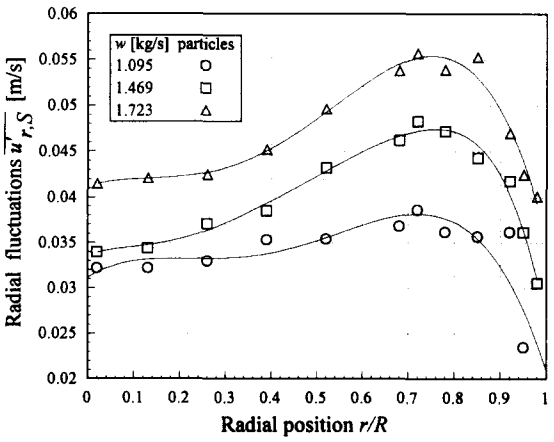


Figure 21. Radial turbulent fluctuations $\overline{u'_{r,S}}$ for the solid phase; solid/liquid flow with ceramic particles.

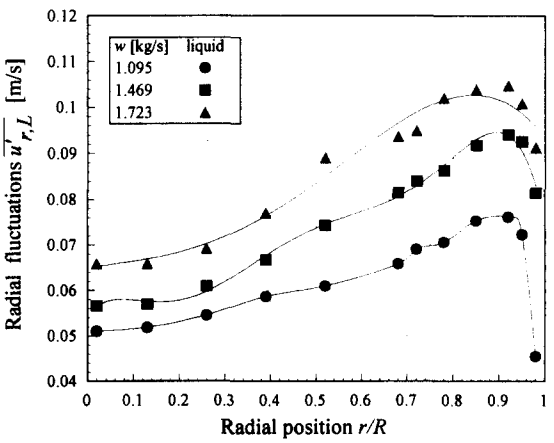


Figure 22. Radial turbulent fluctuations $\overline{u'_{r,L}}$ for the liquid phase; solid/liquid flow with ceramic particles.

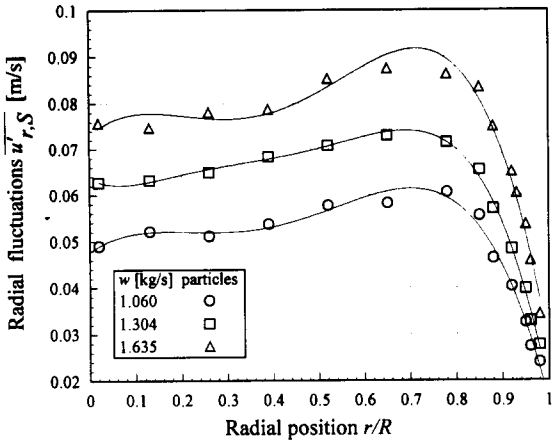


Figure 23. Radial turbulent fluctuations $\overline{u'_{r,S}}$ for the solid phase; solid/liquid flow with expanded polystyrene particles.

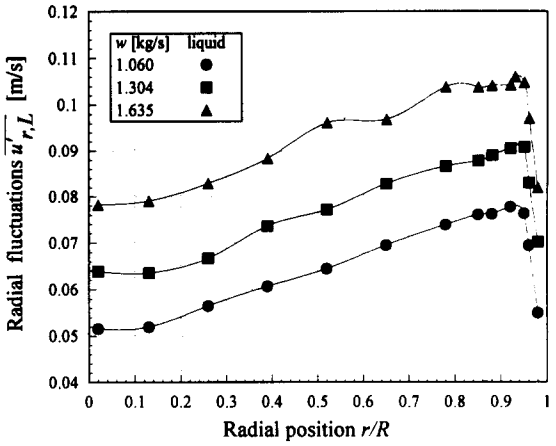


Figure 24. Radial turbulent fluctuations $\overline{u'_{r,L}}$ for the liquid phase; solid/liquid flow with expanded polystyrene particles.

### 3.3. The Turbulence Structure

The measured axial turbulent fluctuations are shown in figures 17–20. The distributions of the turbulence intensities in the axial direction for the liquid phase, $\bar{u}'_{z,L}$ (figures 18 and 20) are quite interesting. There is a sharp increase in the fluctuations near the pipe wall, very probably caused by particle-induced turbulence and vortex shedding behind the particles, which, in general, move faster than the liquid near the wall. Furthermore, we can see in figure 17 that the magnitude of the turbulence intensity in the flow with the ceramic particles does not change much near the pipe's centerline at different flow rates. The same trend is seen for the liquid phase in figure 18. In contrast, a different trend is seen for the flow with expanded polystyrene particles (figures 19 and 20).

The radial turbulent velocity fluctuations, $\bar{u}'_r$, are shown in figures 21–24. Comparing the turbulence intensity distributions at different flow rates, a noticeable change is seen near the pipe's centerline for the flow with both type particles. In addition, if the radial and axial fluctuations for both phases are compared, the conclusion is that, in general, the magnitudes of the particle turbulence intensities are larger for the flow with the expanded polystyrene particles. That is, the turbulent intensity of the heavy ceramic particles, which have relatively large inertia, is damped in comparison with the light polystyrene particles. Interestingly, the liquid phase turbulence is not affected much by the change in particle density. There is, however, a slight decrease in the turbulence level in the flow with the ceramic particles, which seems reasonable because of the larger inertia of these particles.

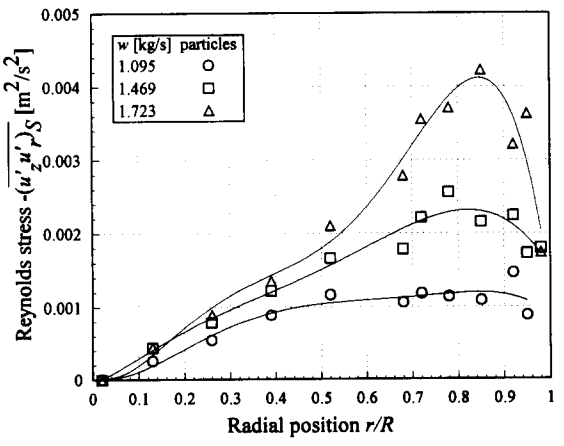


Figure 25. Reynolds stress $-\overline{(u'_z u'_r)_S}$ for the solid phase; solid/liquid flow with ceramic particles.

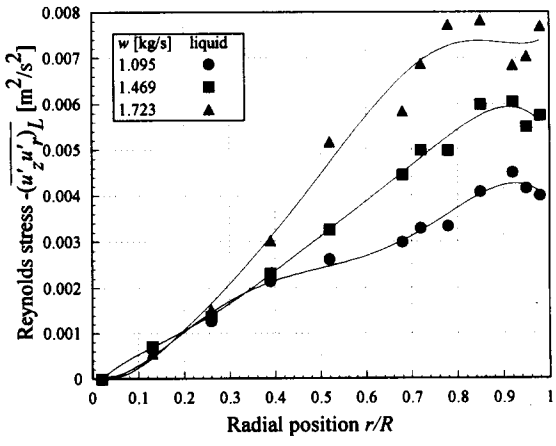


Figure 26. Reynolds stress $-\overline{(u'_z u'_r)_L}$ for the liquid phase; solid/liquid flow with ceramic particles.

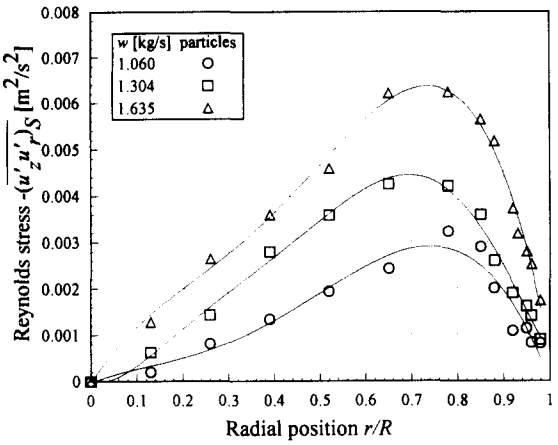


Figure 27. Reynolds stress $-(\overline{u'_z u'_r})_S$ for the solid phase; solid/liquid flow with expanded polystyrene particles.

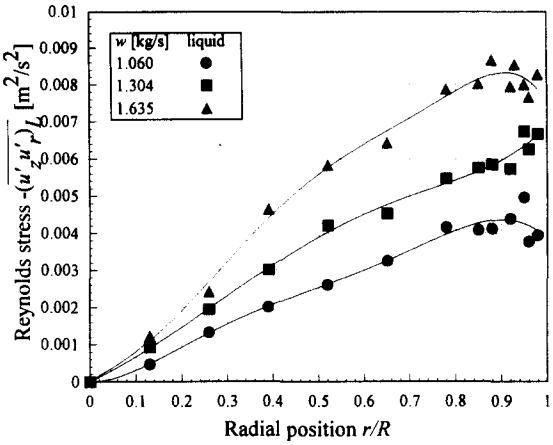


Figure 28. Reynolds stress $-(\overline{u'_z u'_r})_L$ for the liquid phase; solid/liquid flow with expanded polystyrene particles.

The measured Reynolds stresses, $\overline{u'_z u'_r}$, are displayed in figures 25–28. By comparing the magnitude of the Reynolds stress distributions for the flow with the ceramic particles and the expanded polystyrene particles, the same conclusions are reached as before; the Reynolds stresses of the solid phase are larger for the flows with the expanded polystyrene particles.

## 4. SUMMARY AND CONCLUSIONS

A method has been developed which uses an LDA system for volume fraction measurements in solid/fluid flow. The method is valid for dilute concentrations of spherical particles, which are much larger than the fluid's seeding, and where the spatial changes in the particle concentration, $n''$, can be linearized in the immediate vicinity of the particles. It consists of correction procedures which account for the biases in the measured time fractions used to calculate the volume fraction. These biases are caused by the presence of the natural seeding, the finite measurement volume size and beam interruptions.

The clearly visible separation of the large particles from the seeding made the first effect negligibly small. This separation is based on the large difference between the sizes of the seeding and the dispersed particles.

A correction coefficient was introduced which accounts for the finite size of the measurement volume. A single-beam $\gamma$-ray densitometer was used as a calibration device in its calculation. The method is based on the assumption that the size of the measurement volume does not vary with the radial position. The analyses of the interaction physics between the large particles and the measurement volume gave a criterion, which should be applied to test the plausibility of this assumption for any set of experimental data. The correction coefficient is a function of the particle properties. Therefore, it requires new calibration by the $\gamma$-densitometer for each new set of the particles.

The model for the correction due to beam interruptions accounts for the possibility of many particles interrupting the laser beams at the same time. It requires a known size distribution of the particles in use, which should be measured for each new set of particles used. The standard deviation from the mean particle size was used to estimate the error in the correction procedure. It gives the reliability of the whole procedure and should be carefully calculated each time the method is employed.

Detailed measurements of the phase distribution and turbulence structure for solid/fluid upflow in a pipe were made. The particles used were ceramic and expanded polystyrene particles. The velocity, turbulence intensity and Reynolds stresses were measured using a two-dimensional LDA. The LDA system allowed for accurate measurements of both the solid- and liquid-phase velocities. The local volume fraction was measured with an LDA system, and was calibrated against a single-beam $\gamma$-ray densitometer. The corrected volume fraction profiles for the ceramic particles show an almost uniform distribution across the pipe cross section at low liquid flows, while particle

coring was observed at higher liquid flow rates. These trends are in basic agreement with the data obtained by Akagawa *et al.* (1989) and Sakaguchi *et al.* (1991). In contrast, wall peaking was observed for expanded polystyrene particles.

*Acknowledgements*—The authors wish to acknowledge the financial support given to this research by the National Science Foundation. In addition, the advice and help given to this project by Dr N. Takenaka (Kobe University, Japan) is gratefully acknowledged.

## REFERENCES

AKAGAWA, K., FUJII, T. & TAKENAKA, N., 1989, "The effects of the density ratio in a vertically rising solid-liquid two-phase flow," Proc. of the International Conference on Mechanics of Two-phase Flows, National Taiwan University, Taipei, Taiwan, 203–208.

BRAYTON, D. B., KALB, H. T. & CROSSWY, F. L., 1973, "Two-Component Dual-Scatter Laser Doppler Velocimeter with Frequency Burst Signal Readout," *Appl. Opt.*, **12,** 1145–1156.

BRAYTON, D. B., 1974, "Small Particle Signal Characteristics of a Dual-Scatter Laser Velocimeter," *Appl. Opt.*, **13,** 2346–2351.

DANTEC, 1989, *Particle Dynamics Analyzer, User's Manual*, Scientific Research Equipment Division, Dantec Information Department.

DURST, F. & ZARÉ, M., 1975, "Laser-Doppler Measurements in Two-Phase Flows. The Accuracy of Flow Measurement by Laser-Doppler Methods," LDA-Symp., Copenhagen, 403–429.

DURST, F., MELLING, A. & WHITELAW, J. H., 1981, *Principles and Practice of Laser-Doppler Anemometry*. Academic Press, London.

DURRANI, T. S. & GREATED, C. A., 1977, *Laser Systems in Flow Measurement*. Plenum Press, New York.

FARMER, W. M. & BRAYTON, D. B., 1971, "Analysis of Atmospheric Laser Doppler Velocimeters," *Appl. Opt.*, **10,** 2319–2324.

FARMER, W. M., 1972, "Measurement of Particle Size, Number Density, and Velocity Using a Laser Interferometer," *Appl. Opt.*, **11,** 2603–2512.

FARMER, W. M., 1974, "Observation of Large Particles with a Laser Interferometer," *Appl. Opt.*, **13,** 610–622.

FARMER, W. M., 1980, "Visibility of Large Spheres Observed with Laser Velocimeter: a Simple Model," *Appl. Opt.*, **19,** 3660–3667.

KOGELINK, H., 1965, "Imaging of Optical Modes—Resonators with Internal Lenses," *Bell Syst. Tech.*, **44,** 455–494.

LEE, S. J. & DURST, F., 1982, "On the Motion of Particles in Turbulent Duct Flows," *Int. J. Multiphase Flow*, **8**(2), 125–146.

MARIÉ, J. L. & LANCE, M., 1984, "Turbulence Measurements in Two-Phase Bubbly Flows Using Laser Doppler Anemometry," Measuring Techniques in Gas-Liquid Two-Phase Flows, IUTAM Symposium Nancy, France, Editors: Delhaye, J. M, Cognet, G., Springer Verlag, Berlin, 141–148.

QIU, H. H., SOMMERFELD, M. & DURST, F., 1991, "High-Resolution Data Processing for Phase-Doppler Measurements in a Complex Two-Phase Flow," *Meas. Sci. Technol.*, **2,** 455–463.

SAFFMAN, M., 1987, "Automatic Calibration of LDA Measurement Volume Size," *Appl. Opt.*, **26,** 2592–2597.

SAKAGUCHI, T., SHAKUTSI, H., TOMIYAMA, A., MINIGAWA, H. & KITANI, S., 1991, "Microscopic characteristic of multiphase flow using digital image processing," Proceedings of The International Conference on Multiphase Flows '91 Tsukuba, Tsukuba, Japan, 357–360.

SERIZAWA, A., 1974. "Fluid-dynamic characteristics of two-phase flow," Ph.D. Thesis, Kyoto Univ., Japan.

SOMMERFELD, M. & QIU, H. H., 1991, "Detailed Measurements in a Swirling Particulate Two-Phase Flow by a Phase-Doppler Anemometer," *Int. J. Heat and Fluid Flow*, **12,** 20–28.

SCHROCK, V. E., 1969, "Radiation Attenuation Techniques in Two-Phase Flow Measurement," ASME Symposium Volume, Two-Phase Flow Instrumentation.

YU, P. Y. W. & VARTY, R. L., 1988, "Laser-Doppler Measurement of the Velocity and Diameter of Bubbles Using the Triple-Peak Technique," *Int. J. Multiphase Flow*, **14**, 765–776.

WANG, S. K., LEE, S. J., JONES, O. C. & LAHEY, R. T., JR., 1987, "3-D Turbulence Structure and Phase Distribution Measurements in Bubbly Two-Phase Flow," *Int. J. Multiphase Flow*, **13**(3), 327–343.

WIGLEY, G., 1978, "The Sizing of Large Droplets by Laser Anemometry," *J. Phys. E: Scient. Instrum.*, **11**, 639–642.

ŽUN, I., 1985, "The role of void peaking in vertical two-phase bubbly flow," In Proc. of The 2nd International Conference on Multi-phase Flow, London, England, 127–139.

## APPENDIX A

Assuming that the two-phase mixture is well-mixed, and the attenuation of the $\gamma$-beam in air is neglected, the beam intensity measured by the detector is

$$I = I_0 \exp(-2\mu_W W)\exp\{-[\mu_L + \bar{\epsilon}_S(\mu_S - \mu_L)]L\}, \quad [A1]$$

where $I_0$ is the unattenuated beam intensity, $W$ is the wall thickness, $L$ is the chord length of the pipe at the centerline (both quantities in cm), $\mu_W$, $\mu_L$ and $\mu_S$ are the macroscopic attenuation cross sections for the wall, liquid and solid phase, respectively (all in $cm^{-1}$). The beam intensity, measured by the detector, with liquid only in the pipe is

$$I_L = I_0 \exp(-2\mu_W W)\exp(-\mu_L L). \quad [A2]$$

Similarly, for the case of the mixture with the maximum possible concentration of particles, $\bar{\epsilon}_{S0}$, the $\gamma$-beam intensity is

$$I_{SL} = I_0 \exp(-2\mu_W W)\exp\{-[\mu_L + \bar{\epsilon}_{S0}(\mu_S - \mu_L)]L\}. \quad [A3]$$

Dividing [A1] by [A2] gives

$$\frac{I}{I_L} = \exp[-\bar{\epsilon}_S(\mu_S - \mu_L)L]. \quad [A4]$$

Similarly, the ratio between [A3] and [A2] leads to

$$\frac{I_{SL}}{I_L} = \exp[-\bar{\epsilon}_{S0}(\mu_S - \mu_L)L]. \quad [A5]$$

Taking the natural logarithm of [A4] and [A5] and then rearranging their ratio, yields

$$\bar{\epsilon}_S = \bar{\epsilon}_{S0}\frac{\ln\left(\frac{I}{I_L}\right)}{\ln\left(\frac{I_{SL}}{I_L}\right)}. \quad [A6]$$

The error in $\bar{\epsilon}_S$ is obtained by a "propagation-of-error" analysis:

$$(\Delta\bar{\epsilon}_S)^2 = \left(\frac{\partial\bar{\epsilon}_S}{\partial\bar{\epsilon}_{S0}}\right)^2(\Delta\bar{\epsilon}_{S0})^2 + \left(\frac{\partial\bar{\epsilon}_S}{\partial I}\right)^2(\Delta I)^2 + \left(\frac{\partial\bar{\epsilon}_S}{\partial I_L}\right)^2(\Delta I_L)^2 + \left(\frac{\partial\bar{\epsilon}_S}{\partial I_{SL}}\right)^2(\Delta I_{SL})^2. \quad [A7]$$

By using [A6] in [A7] the following result is obtained:

$$\left(\frac{\Delta\bar{\epsilon}_S}{\bar{\epsilon}_S}\right)^2 = \left(\frac{\Delta\bar{\epsilon}_{S0}}{\bar{\epsilon}_{S0}}\right)^2 + \frac{1}{\bar{\epsilon}_S^2\ln\left(\frac{I_{SL}}{I_L}\right)^2}\left[\bar{\epsilon}_{S0}^2\left(\frac{\Delta I}{I}\right)^2 + (\bar{\epsilon}_S - \bar{\epsilon}_{S0})^2\left(\frac{\Delta I_L}{I_L}\right)^2 + \bar{\epsilon}_S^2\left(\frac{\Delta I_{SL}}{I_{SL}}\right)^2\right]. \quad [A8]$$

$I_{SL}$ and $I_{SG}$ need to be measured for establishing the reference chordal volume fraction, $\bar{\epsilon}_{S0}$. The pipe is first filled with the particles, air filling the voids between them. The attenuated intensity $I_{SG}$ for this case is

$$I_{SG} = I_0 \exp(-2\mu_W W)\exp\{-[\mu_G + \bar{\epsilon}_{S0}(\mu_S - \mu_G)]L\}, \quad [A9]$$

where $\mu_G$ is the macroscopic attenuation cross section of the gas. Next, liquid is poured into the pipe, displacing the air, and the intensity is measured at the same spot. The intensity measured corresponds to $I_{SL}$, obtained by [A3]. The ratio between $I_{SL}$ and $I_{SG}$ is then

$$\frac{I_{SL}}{I_{SG}} = \exp[-(1-\bar{\epsilon}_{S0})(\mu_L - \mu_G)L]. \quad [A10]$$

By rearranging, the reference chordal volume fraction, $\bar{\epsilon}_{S0}$, is

$$\bar{\epsilon}_{S0} = 1 + \frac{\ln\left(\frac{I_{SL}}{I_{SG}}\right)}{(\mu_L - \mu_G)L}. \quad [A11]$$

Hence, the error in $\bar{\epsilon}_{S0}$ is estimated to be

$$\left(\frac{\Delta\bar{\epsilon}_{S0}}{\bar{\epsilon}_{S0}}\right)^2 = \left[\frac{1}{(\mu_L - \mu_G)L + \ln\left(\frac{I_{SL}}{I_{SG}}\right)}\right]^2 \left[\left(\frac{\Delta I_{SL}}{I_{SL}}\right)^2 + \left(\frac{\Delta I_{SG}}{I_{SG}}\right)^2 + \ln\left(\frac{I_{SL}}{I_{SG}}\right)^2 \left(\frac{\Delta L}{L}\right)^2\right]. \quad [A12]$$

By assuming a Poisson distribution of the measured counts, the following expression is obtained for the error in the relative intensity:

$$\frac{\Delta I}{I} = \frac{1}{\sqrt{N}}, \quad [A13]$$

where $N$ is the total number of counts.

## APPENDIX B

The position of the measuring volume is at $x$, $y$ and fixed $z$ (the measurements are performed in the $x$–$y$ plane at constant $z$). Figure B1 shows the geometry involved in the calculation. The angle between the beam and the $y$ coordinate is denoted by $\Psi$. The relations between the parameters in Figure B1 are:

$$\gamma = \frac{\pi}{2} - \Psi - \arctan\left(\frac{x}{|y|}\right), \quad [B1]$$

$$d_{MV} = \sqrt{x^2 + y^2}, \quad [B2]$$

$$\eta = \arcsin\left(\frac{d_{MV}}{R}\sin\gamma\right) \quad [B3]$$

and

$$\Phi = \pi - \gamma - \eta. \quad [B4]$$

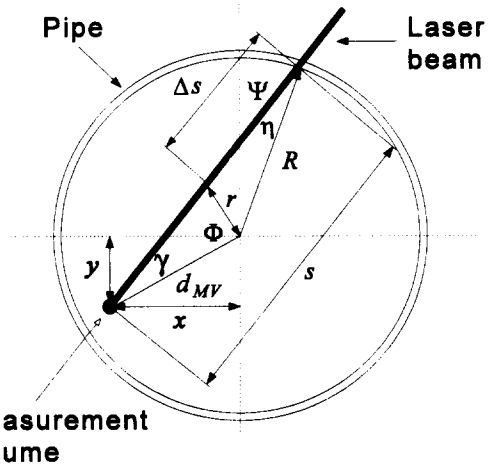


Figure B1. The geometry involved with the calculation of $K_2$.

The length of the beam section in the pipe is

$$s = \frac{R \sin \Phi}{\sin \gamma}. \qquad [B5]$$

If $\Delta s$ in figure B1 represents the length from the wall to a certain location in the beam, that location is at the following distance from the pipe's centerline:

$$r = \sqrt{\Delta s^2 + R^2 - 2\Delta s R \cos \eta}. \qquad [B6]$$

Equations [51] and [57] are evaluated at the location at $r$.

# APPENDIX C

## *Data for the Ceramic Particles*

Table C1. $w = 1.095$ kg/s, $\langle j_L \rangle = 1.410$ m/s and $\langle j_S \rangle = 0.032$ m/s

| $r/R$ | $U_{z,S}$ [m/s] | $U_{z,L}$ [m/s] | $\overline{u'^2_{z,S}} \cdot 10^{-2}$ [m/s] | $\overline{u'^2_{z,L}} \cdot 10^{-2}$ [m/s] | $\overline{u'^2_{r,S}} \cdot 10^{-2}$ [m/s] | $\overline{u'^2_{r,L}} \cdot 10^{-2}$ [m/s] | $-\overline{(u'_z u'_r)_S} \cdot 10^{-4}$ [m$^2$/s$^2$] | $-\overline{(u'_z u'_r)_L} \cdot 10^{-4}$ [m$^2$/s$^2$] | $\epsilon$ [%] | $\epsilon_C$ [%] | $\Delta\epsilon_C$ [%] |
|---|---|---|---|---|---|---|---|---|---|---|---|
| 0.00 | 1.579 | 1.814 | 6.65 | 9.02 | 3.22 | 5.11 | 0.00 | 0.00 | 2.44 | 3.32 | 0.24 |
| 0.13 | 1.571 | 1.808 | 7.07 | 9.32 | 3.22 | 5.19 | 2.56 | 6.54 | 2.54 | 3.42 | 0.25 |
| 0.26 | 1.538 | 1.754 | 7.81 | 10.86 | 3.30 | 5.46 | 5.42 | 12.65 | 2.80 | 3.70 | 0.27 |
| 0.39 | 1.487 | 1.710 | 8.06 | 12.01 | 3.53 | 5.87 | 8.86 | 21.49 | 3.00 | 3.81 | 0.26 |
| 0.52 | 1.429 | 1.623 | 8.55 | 12.88 | 3.54 | 6.10 | 11.65 | 26.21 | 3.46 | 4.08 | 0.25 |
| 0.65 | 1.366 | 1.550 | 8.72 | 13.27 | 3.68 | 6.59 | 10.64 | 29.91 | 3.16 | 3.32 | 0.19 |
| 0.72 | 1.345 | 1.503 | 8.58 | 13.08 | 3.86 | 6.91 | 11.85 | 32.95 | 2.68 | 2.63 | 0.14 |
| 0.78 | 1.317 | 1.438 | 8.77 | 13.05 | 3.62 | 7.07 | 11.42 | 33.39 | 1.72 | 1.60 | 0.08 |
| 0.85 | 1.286 | 1.368 | 8.95 | 13.71 | 3.57 | 7.54 | 10.91 | 40.87 | 0.76 | 0.69 | 0.03 |
| 0.92 | 1.252 | 1.242 | 9.31 | 14.99 | 3.62 | 7.62 | 14.63 | 45.05 | 0.17 | 0.17 | 0.07 |
| 0.95 | 1.240 | 1.144 | 7.58 | 16.86 | 2.35 | 7.24 | 8.88 | 41.59 | 0.05 | 0.05 | 0.01 |
| 0.98 | | 0.861 | | 21.84 | | 4.56 | | 40.01 | | | |

Table C2. $w = 1.469$ kg/s, $\langle j_L \rangle = 1.888$ m/s and $\langle j_S \rangle = 0.045$ m/s

| $r/R$ | $U_{z,S}$ [m/s] | $U_{z,L}$ [m/s] | $\overline{u'^2_{z,S}} \cdot 10^{-2}$ [m/s] | $\overline{u'^2_{z,L}} \cdot 10^{-2}$ [m/s] | $\overline{u'^2_{r,S}} \cdot 10^{-2}$ [m/s] | $\overline{u'^2_{r,L}} \cdot 10^{-2}$ [m/s] | $-\overline{(u'_z u'_r)_S} \cdot 10^{-4}$ [m$^2$/s$^2$] | $-\overline{(u'_z u'_r)_L} \cdot 10^{-4}$ [m$^2$/s$^2$] | $\epsilon$ [%] | $\epsilon_C$ [%] | $\Delta\epsilon_C$ [%] |
|---|---|---|---|---|---|---|---|---|---|---|---|
| 0.00 | 2.145 | 2.329 | 7.23 | 10.31 | 3.40 | 5.66 | 0.00 | 0.00 | 3.83 | 5.45 | 0.42 |
| 0.13 | 2.130 | 2.333 | 7.44 | 10.05 | 3.44 | 5.70 | 4.41 | 7.07 | 3.87 | 5.43 | 0.41 |
| 0.26 | 2.087 | 2.317 | 8.36 | 10.96 | 3.71 | 6.10 | 7.87 | 13.74 | 4.03 | 5.36 | 0.39 |
| 0.39 | 2.054 | 2.270 | 9.58 | 12.20 | 3.85 | 6.68 | 12.22 | 23.19 | 3.67 | 4.51 | 0.29 |
| 0.52 | 1.994 | 2.184 | 10.50 | 14.24 | 4.32 | 7.43 | 16.61 | 32.63 | 3.41 | 3.79 | 0.22 |
| 0.65 | 1.923 | 2.089 | 10.59 | 15.64 | 4.62 | 8.16 | 17.84 | 44.56 | 2.53 | 2.52 | 0.13 |
| 0.72 | 1.891 | 2.032 | 10.70 | 16.46 | 4.83 | 8.41 | 22.14 | 49.89 | 1.82 | 1.73 | 0.09 |
| 0.78 | 1.839 | 1.911 | 11.90 | 17.10 | 4.72 | 8.64 | 25.61 | 49.85 | 1.11 | 1.03 | 0.05 |
| 0.85 | 1.785 | 1.799 | 11.86 | 17.78 | 4.43 | 9.19 | 21.55 | 59.90 | 0.59 | 0.53 | 0.03 |
| 0.92 | 1.699 | 1.662 | 12.13 | 18.19 | 4.18 | 9.42 | 22.43 | 60.50 | 0.21 | 0.19 | 0.01 |
| 0.95 | 1.660 | 1.559 | 11.76 | 19.52 | 3.62 | 9.27 | 17.24 | 55.04 | 0.08 | 0.07 | 0.01 |
| 0.98 | 1.585 | 1.272 | 12.07 | 25.39 | 3.06 | 8.16 | 18.00 | 57.51 | | | |

Table C3. $w = 1.723$ kg/s, $\langle j_L \rangle = 2.196$ m/s and $\langle j_S \rangle = 0.060$ m/s

| $r/R$ | $U_{z,S}$ [m/s] | $U_{z,L}$ [m/s] | $\overline{u'^2_{z,S}} \cdot 10^{-2}$ [m/s] | $\overline{u'^2_{z,L}} \cdot 10^{-2}$ [m/s] | $\overline{u'^2_{r,S}} \cdot 10^{-2}$ [m/s] | $\overline{u'^2_{r,L}} \cdot 10^{-2}$ [m/s] | $-\overline{(u'_z u'_r)_S} \cdot 10^{-4}$ [m$^2$/s$^2$] | $-\overline{(u'_z u'_r)_L} \cdot 10^{-4}$ [m$^2$/s$^2$] | $\epsilon$ [%] | $\epsilon_C$ [%] | $\Delta\epsilon_C$ [%] |
|---|---|---|---|---|---|---|---|---|---|---|---|
| 0.00 | 2.666 | 2.832 | 6.66 | 11.58 | 4.15 | 6.59 | 0.00 | 0.00 | 4.60 | 6.93 | 0.57 |
| 0.13 | 2.650 | 2.817 | 7.11 | 11.74 | 4.21 | 6.60 | 4.43 | 5.60 | 4.62 | 6.80 | 0.54 |
| 0.26 | 2.613 | 2.760 | 8.63 | 12.37 | 4.25 | 6.93 | 8.96 | 15.22 | 4.50 | 6.18 | 0.46 |
| 0.39 | 2.553 | 2.683 | 9.85 | 13.81 | 4.52 | 7.71 | 13.51 | 30.28 | 3.97 | 4.94 | 0.33 |
| 0.52 | 2.467 | 2.537 | 11.62 | 16.54 | 4.96 | 8.91 | 21.01 | 51.78 | 3.40 | 3.79 | 0.22 |
| 0.65 | 2.404 | 2.440 | 12.55 | 18.33 | 5.38 | 9.38 | 27.85 | 58.48 | 2.30 | 2.31 | 0.12 |
| 0.72 | 2.331 | 2.348 | 14.08 | 20.11 | 5.57 | 9.50 | 35.51 | 68.78 | 1.78 | 1.71 | 0.09 |
| 0.78 | 2.266 | 2.227 | 14.80 | 21.13 | 5.39 | 10.22 | 37.09 | 77.33 | 1.21 | 1.14 | 0.06 |
| 0.85 | 2.179 | 2.099 | 15.94 | 21.96 | 5.53 | 10.40 | 42.23 | 78.22 | 0.84 | 0.76 | 0.04 |
| 0.92 | 2.051 | 1.901 | 16.04 | 21.84 | 4.70 | 10.49 | 32.10 | 68.51 | 0.39 | 0.34 | 0.02 |
| 0.95 | 1.984 | 1.761 | 15.72 | 22.44 | 4.25 | 10.09 | 36.27 | 70.39 | 0.17 | 0.16 | 0.01 |
| 0.98 | 1.851 | 1.423 | 13.98 | 27.40 | 4.01 | 9.14 | 17.39 | 76.98 | | | |

# APPENDIX D

## *Data for the Expanded Polystyrene Particles*

Table D1. $w = 1.060$ kg/s, $\langle j_L \rangle = 1.441$ m/s and $\langle j_S \rangle = 0.022$ m/s

| $r/R$ | $U_{z,S}$ [m/s] | $U_{z,L}$ [m/s] | $\overline{u'^2_{z,S}}\cdot 10^{-2}$ [m/s] | $\overline{u'^2_{z,L}}\cdot 10^{-2}$ [m/s] | $\overline{u'^2_{r,S}}\cdot 10^{-2}$ [m/s] | $\overline{u'^2_{r,L}}\cdot 10^{-2}$ [m/s] | $-\overline{(u'_z u'_r)_S}\cdot 10^{-4}$ [m$^2$/s$^2$] | $-\overline{(u'_z u'_r)_L}\cdot 10^{-4}$ [m$^2$/s$^2$] | $\epsilon$ [%] | $\epsilon_C$ [%] | $\Delta\epsilon_C$ [%] |
|---|---|---|---|---|---|---|---|---|---|---|---|
| 0.00 | 1.996 | 1.815 | 10.23 | 8.83 | 4.90 | 5.16 | 0.00 | 0.00 | 1.05 | 1.13 | 0.20 |
| 0.13 | 1.989 | 1.815 | 11.07 | 8.98 | 5.21 | 5.20 | 1.96 | 4.74 | 1.05 | 1.13 | 0.19 |
| 0.26 | 1.947 | 1.790 | 11.74 | 8.94 | 5.11 | 5.65 | 8.10 | 13.33 | 1.14 | 1.20 | 0.21 |
| 0.39 | 1.875 | 1.732 | 12.03 | 10.12 | 5.37 | 6.07 | 13.35 | 20.17 | 1.21 | 1.27 | 0.21 |
| 0.52 | 1.798 | 1.656 | 12.69 | 11.35 | 5.77 | 6.45 | 19.33 | 26.15 | 1.29 | 1.33 | 0.22 |
| 0.65 | 1.701 | 1.570 | 12.91 | 12.56 | 5.82 | 6.95 | 24.22 | 32.52 | 1.34 | 1.34 | 0.21 |
| 0.78 | 1.542 | 1.431 | 14.50 | 14.30 | 6.06 | 7.39 | 32.26 | 41.67 | 1.44 | 1.38 | 0.21 |
| 0.85 | 1.428 | 1.344 | 13.60 | 14.60 | 5.55 | 7.61 | 28.95 | 40.87 | 1.55 | 1.48 | 0.22 |
| 0.88 | 1.347 | 1.289 | 12.75 | 14.63 | 4.64 | 7.62 | 20.02 | 41.29 | 2.29 | 2.08 | 0.30 |
| 0.92 | 1.307 | 1.270 | 12.23 | 15.18 | 4.03 | 7.78 | 10.79 | 43.96 | 2.63 | 2.21 | 0.31 |
| 0.95 | 1.214 | 1.169 | 12.37 | 16.45 | 3.26 | 7.63 | 11.37 | 49.68 | 2.12 | 1.69 | 0.21 |
| 0.96 | 1.150 | 1.082 | 12.25 | 17.93 | 2.74 | 6.94 | 8.21 | 37.80 | 1.45 | 1.16 | 0.15 |
| 0.98 | 1.065 | 0.918 | 12.88 | 20.85 | 2.40 | 5.50 | 8.12 | 39.53 | 0.78 | 0.83 | 0.10 |

Table D2. $w = 1.304$ kg/s, $\langle j_L \rangle = 1.772$ m/s and $\langle j_S \rangle = 0.023$ m/s

| $r/R$ | $U_{z,S}$ [m/s] | $U_{z,L}$ [m/s] | $\overline{u'^2_{z,S}}\cdot 10^{-2}$ [m/s] | $\overline{u'^2_{z,L}}\cdot 10^{-2}$ [m/s] | $\overline{u'^2_{r,S}}\cdot 10^{-2}$ [m/s] | $\overline{u'^2_{r,L}}\cdot 10^{-2}$ [m/s] | $-\overline{(u'_z u'_r)_S}\cdot 10^{-4}$ [m$^2$/s$^2$] | $-\overline{(u'_z u'_r)_L}\cdot 10^{-4}$ [m$^2$/s$^2$] | $\epsilon$ [%] | $\epsilon_C$ [%] | $\Delta\epsilon_C$ [%] |
|---|---|---|---|---|---|---|---|---|---|---|---|
| 0.00 | 2.403 | 2.265 | 11.77 | 10.76 | 6.27 | 6.39 | 0.00 | 0.00 | 0.97 | 1.01 | 0.17 |
| 0.13 | 2.385 | 2.254 | 12.06 | 10.77 | 6.32 | 6.36 | 6.28 | 9.22 | 1.01 | 1.05 | 0.17 |
| 0.26 | 2.339 | 2.208 | 13.47 | 12.42 | 6.49 | 6.67 | 14.38 | 19.53 | 1.07 | 1.10 | 0.18 |
| 0.39 | 2.257 | 2.129 | 14.82 | 14.56 | 6.84 | 7.36 | 27.93 | 30.21 | 1.15 | 1.17 | 0.19 |
| 0.52 | 2.160 | 2.036 | 15.84 | 16.70 | 7.08 | 7.72 | 35.80 | 42.09 | 1.22 | 1.22 | 0.20 |
| 0.65 | 2.043 | 1.906 | 16.65 | 16.37 | 7.31 | 8.28 | 42.48 | 45.34 | 1.29 | 1.26 | 0.20 |
| 0.78 | 1.876 | 1.772 | 16.01 | 16.90 | 7.16 | 8.66 | 42.11 | 54.65 | 1.40 | 1.30 | 0.19 |
| 0.85 | 1.752 | 1.665 | 15.24 | 17.28 | 6.55 | 8.78 | 35.93 | 57.59 | 1.46 | 1.33 | 0.19 |
| 0.88 | 1.696 | 1.607 | 14.97 | 17.65 | 5.71 | 8.90 | 25.96 | 58.53 | 1.81 | 1.60 | 0.23 |
| 0.92 | 1.620 | 1.527 | 14.73 | 17.80 | 4.84 | 9.06 | 19.00 | 57.32 | 2.04 | 1.65 | 0.23 |
| 0.95 | 1.523 | 1.420 | 14.79 | 19.66 | 3.99 | 9.08 | 16.18 | 67.43 | 1.47 | 1.17 | 0.15 |
| 0.96 | 1.438 | 1.309 | 14.74 | 21.92 | 3.30 | 8.30 | 14.10 | 62.60 | 0.98 | 0.78 | 0.10 |
| 0.98 | 1.322 | 1.071 | 14.48 | 24.51 | 2.78 | 7.01 | 8.95 | 66.74 | 0.47 | 0.44 | 0.06 |

Table D3. $w = 1.635$ kg/s, $\langle j_L \rangle = 2.222$ m/s and $\langle j_S \rangle = 0.031$ m/s

| $r/R$ | $U_{z,S}$ [m/s] | $U_{z,L}$ [m/s] | $\overline{u'^2_{z,S}}\cdot 10^{-2}$ [m/s] | $\overline{u'^2_{z,L}}\cdot 10^{-2}$ [m/s] | $\overline{u'^2_{r,S}}\cdot 10^{-2}$ [m/s] | $\overline{u'^2_{r,L}}\cdot 10^{-2}$ [m/s] | $-\overline{(u'_z u'_r)_S}\cdot 10^{-4}$ [m$^2$/s$^2$] | $-\overline{(u'_z u'_r)_L}\cdot 10^{-4}$ [m$^2$/s$^2$] | $\epsilon$ [%] | $\epsilon_C$ [%] | $\Delta\epsilon_C$ [%] |
|---|---|---|---|---|---|---|---|---|---|---|---|
| 0.00 | 2.946 | 2.818 | 14.67 | 12.99 | 7.58 | 7.83 | 0.00 | 0.00 | 1.08 | 1.14 | 0.19 |
| 0.13 | 2.921 | 2.800 | 15.41 | 13.77 | 7.48 | 7.91 | 12.81 | 12.30 | 1.13 | 1.20 | 0.21 |
| 0.26 | 2.880 | 2.759 | 16.64 | 14.96 | 7.81 | 8.29 | 26.44 | 24.32 | 1.24 | 1.29 | 0.22 |
| 0.39 | 2.794 | 2.663 | 18.25 | 17.71 | 7.87 | 8.84 | 35.95 | 46.52 | 1.27 | 1.31 | 0.22 |
| 0.52 | 2.683 | 2.545 | 19.38 | 19.70 | 8.53 | 9.62 | 45.85 | 58.37 | 1.35 | 1.36 | 0.22 |
| 0.65 | 2.549 | 2.408 | 20.38 | 20.52 | 8.75 | 9.69 | 62.05 | 64.31 | 1.38 | 1.35 | 0.21 |
| 0.78 | 2.351 | 2.230 | 21.03 | 22.01 | 8.63 | 10.39 | 62.33 | 78.84 | 1.53 | 1.41 | 0.20 |
| 0.85 | 2.230 | 2.105 | 20.31 | 22.64 | 8.35 | 10.38 | 56.43 | 80.33 | 1.51 | 1.36 | 0.19 |
| 0.88 | 2.150 | 2.025 | 20.50 | 22.87 | 7.51 | 10.42 | 51.67 | 86.75 | 1.77 | 1.53 | 0.21 |
| 0.92 | 2.053 | 1.911 | 19.42 | 22.80 | 6.51 | 10.43 | 37.18 | 79.64 | 1.68 | 1.36 | 0.18 |
| 0.93 | 2.012 | 1.863 | 19.65 | 22.44 | 6.05 | 10.61 | 31.84 | 85.55 | 1.39 | 1.14 | 0.15 |
| 0.95 | 1.955 | 1.773 | 18.72 | 22.98 | 5.37 | 10.48 | 27.90 | 80.12 | 1.07 | 0.86 | 0.11 |
| 0.96 | 1.887 | 1.626 | 18.68 | 23.89 | 4.60 | 9.71 | 25.19 | 76.73 | 0.68 | 0.55 | 0.07 |
| 0.98 | 1.788 | 1.327 | 16.90 | 28.92 | 3.44 | 8.19 | 17.39 | 82.92 | 0.30 | 0.24 | 0.03 |